Cell Reports
Physical Science

Article

Multi-junction laser power converters exceeding 50% efficiency in the short wavelength infrared

Graphical abstract

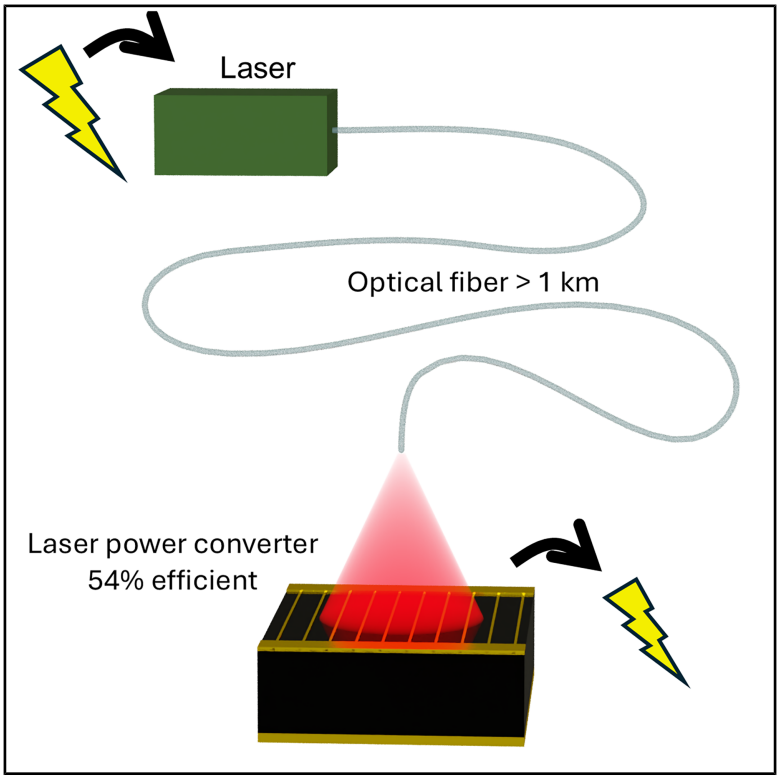

Authors

Gavin P. Forcade, D. Paige Wilson, Meghan N. Beattie, ..., Alexandre W. Walker, Jacob J. Krich, Karin Hinzer

Correspondence

khinzer@uottawa.ca

In brief

The work addresses a critical challenge in laser-based power transmission systems: the low efficiency and output voltage of receivers operating within the optical fiber transmission window. Using a predictive model, Forcade et al. design a receiver that converts 1,446 nm laser light into electrical power with an efficiency of 53.6%.

Highlights

- Can achieve 53.6% efficiency with model-predicted 4-junction laser power converter
- Layer thicknesses can be extracted with one non-destructive measurement
- Can have higher efficiencies for laser power converters with larger bandgaps
- Designs optimized with luminescent coupling surpass absorption-matched designs

Forcade et al., 2025, Cell Reports Physical Science 6, 102610
June 18, 2025
https://doi.org/10.1016/j.xcrp.2025.102610

CellPress

Cell Reports
Physical Science

CellPress
OPEN ACCESS

Article

Multi-junction laser power converters exceeding 50% efficiency in the short wavelength infrared

Gavin P. Forcade,[1] D. Paige Wilson,[2] Meghan N. Beattie,[2] Carmine Pellegrino,[3] Henning Helmers,[3] Robert F.H. Hunter,[2] Oliver Höhn,[3] David Lackner,[3] Louis-Philippe St-Arnaud,[2] Thomas N.D. Tibbits,[3] Daniel Poitras,[5] Christopher E. Valdivia,[2] Yuri Grinberg,[2,4] Alexandre W. Walker,[1,5] Jacob J. Krich,[1] and Karin Hinzer[1,2,6,*]

[1]Department of Physics, University of Ottawa, Ottawa, ON K1N 7P9, Canada
[2]SUNLAB, School of Electrical Engineering and Computer Sciences, University of Ottawa, Ottawa, ON K1N 7P9, Canada
[3]Fraunhofer Institute for Solar Energy Systems ISE, 79110 Freiburg, Germany
[4]Digital Technologies Research Center, National Research Council of Canada, Ottawa, ON K1K 4P7, Canada
[5]Quantum and Nanotechnologies Research Center, National Research Council of Canada, Ottawa, ON K1K 4P7, Canada
[6]Lead contact
*Correspondence: khinzer@uottawa.ca
https://doi.org/10.1016/j.xcrp.2025.102610

SUMMARY

Photonic or laser power converters are crucial components in power-by-light systems. However, their use in long-distance applications has been hindered by low efficiencies and output voltages within the optical fiber transmission window of 1.3–1.6 μm laser wavelengths. Here, we improve and simplify the design and characterization processes for photonic power converters, exceeding 50% efficiency under 1.446 μm laser light. We develop a calibrated model predicting efficiency gains with increasing bandgap, reaching up to 57% efficiency at a 1.3-μm wavelength. As a first demonstration, we produce a high-efficiency device designed by the model: a four-junction InGaAsP photonic power converter with a conversion efficiency of 53.6% ± 1.3% and an output voltage above 2 V under 15.2 W/cm^2 of 1.446 μm laser light. These advances open new, practical pathways for integrating photonic power converters into telecommunication systems and unlock the potential to further optimize their design with machine learning algorithms trained with our predictive model.

INTRODUCTION

Power-by-light systems[1,2] benefit from end-to-end electrical and galvanic isolation and are safer and more secure than conventional electrical power transmission. For instance, power-by-light systems can be helpful for reducing risk of fires or explosions,[3] preventing malfunction near high voltages,[4,5] remote powering of rechargeable batteries,[6] space exploration,[7] and powering 5G technologies.[8,9] They can be used to transmit photonic power and data simultaneously.[3,5,10–12]

Typically, power-by-light systems transmit laser light to a photonic power converter (PPC),[1,2] sometimes called a laser power converter. PPCs are photovoltaic cells that convert monochromatic light into electrical power. They are designed to produce the operating voltages needed to power electrical devices such as 1.8 V, 3.3 V, or 5 V.[13] These voltages are larger than the open-circuit voltage of any single-junction photovoltaic device. The most effective method of achieving such an output voltage is using the III-V semiconductor-based multi-junction architecture, consisting of an epitaxially grown stack of *p-n* junctions interconnected with tunnel diodes.[2,13–16] However, multi-junction cells have demonstrated greater wavelength sensitivity compared with single-junction devices due to current matching constraints,[2,17,18] which must be accounted for in system designs. This paper presents a high-efficiency multi-junction PPC, designed by a model calibrated with single- and 10-junction PPCs and conceived through an exploration of the PPC design space, as summarized in Figure 1A.

When designing PPCs, maximizing the optical-to-electrical power conversion efficiency is crucial. Tuning the laser wavelength and the bandgap of the PPC's absorber material can minimize thermalization, transparency, and current collection losses. For long-distance power transmission through optical fibers, laser wavelengths within 1.3–1.6 μm (see Figure 1B) minimize attenuation losses.[19] For applications with negligible transmission losses, 1 μm lasers may be of interest due to their high lasing efficiency.[20] Therefore, we employ absorber materials composed of InGaAsP (bandgap 0.736–1.215 eV) lattice-matched to InP to cover this range.[21] So far, single-junction PPCs using this material have achieved efficiencies up to 52.8% at 1.31 μm,[22] but suffer from low output voltages of 0.6 V. Multi-junction PPCs with InGaAs (bandgap 0.736 eV) absorber layers designed for a 1.47 μm wavelength have achieved efficiencies up to 67.5% when cooled to 77 K[23] but have yet to reach efficiencies above 50% when operating at room temperature.[13] Since the bandgap-voltage offset is effectively constant

Please cite this article in press as: Forcade et al., Multi-junction laser power converters exceeding 50% efficiency in the short wavelength infrared, Cell Reports Physical Science (2025), https://doi.org/10.1016/j.xcrp.2025.102610

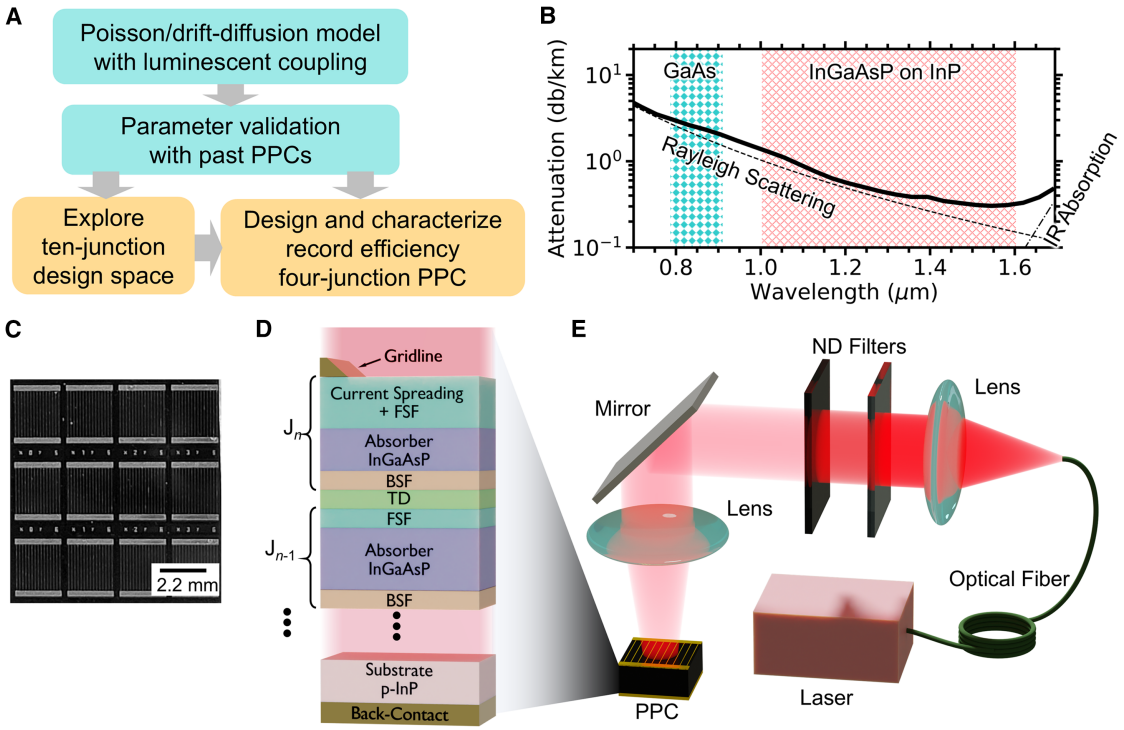

Figure 1. Photonic power converter device structure and measurement setup

(A) Block diagram providing an overview of the paper.

(B) Attenuation of light's electromagnetic spectrum within an optical fiber, highlighting in red mesh the range of wavelengths targeted in this study. Our target corresponds to the frequency range (1.9–3) $\times$ 10^{14} Hz, which is equivalent to a photon energy range of 0.736–1.215 eV.

(C) Top-view photograph of our 2.2 $\times$ 2.9-mm^2 photonic power converter (PPC) chips, the designated area (mesa minus busbar area) is 0.054 cm^2. The scale bar is 2.2-mm wide.

(D) Schematic cross-section of the multi-junction PPC, which is composed of junctions containing InGaAsP absorber layers cladded with larger bandgap front and back surface field (FSF and BSF) layers. The *n* junctions are connected in series with tunnel diodes (TDs).

(E) Schematic diagram of the PPC measurement setup.

with bandgap for InGaAsP photovoltaic devices,[24] higher efficiencies can be achieved with larger bandgap absorber layers. We present a four-junction PPC with InGaAsP (bandgap 0.8 eV) absorber layers that surpasses the 50% efficiency barrier at 1.446 μm. This achievement was realized through rigorous design optimization using a comprehensive model.

Various techniques have been used to model PPCs,[25–27] providing different pathways to optimization. Friedman et al.[28] predicted enhanced efficiencies of high-quality photovoltaic devices beyond the absorption-matching thicknesses by optimizing devices while considering luminescent coupling[17,29,30]—radiative recombination that is reabsorbed in different junctions. Xia and Krich[26] presented a detailed-balance model including luminescent coupling and parametrized all nonradiative processes through an internal radiative efficiency but omitted optical interference effects arising from changes in refractive indices between layers, as well as realistic electrical transport effects. We employ a calibrated drift-diffusion model that includes luminescent coupling, optical interference effects, and realistic charge transport, which promises more accurate predictions at the cost of being more computationally expensive[31,32] than both Friedman[28] and Xia[26] models.

To maximize the integration of power-by-light systems into telecom infrastructure, it is desirable to use the same fiber for simultaneous power and data transmission. However, this dual-use fiber configuration requires using different wavelengths to avoid negatively impacting data quality[9,33]; it is, therefore, essential to understand PPC performance vs. wavelength. We use our model within the corresponding 1.0–1.6 μm laser wavelength range (see Figure 1B) and predict attainable efficiencies up to 67%, with efficiency increasing with absorber bandgap. Within the optical fiber transmission window (1.3–1.6 μm), we anticipate efficiencies of up to 57%. We perform a sensitivity analysis, varying laser wavelength and absorber material bandgap to investigate the tolerance of optimized PPC efficiency to operational conditions and epitaxial variations.

We present the optoelectronic properties of processed single-, four-, and 10-junction PPCs. The single- and 10-junction PPCs, featuring $In_{0.53}Ga_{0.47}As$ (bandgap 0.736 eV) absorber layers, are introduced in the section "10-junction InGaAs/InP PPC". A technique to non-destructively determine multi-junction PPC absorber thicknesses with a single measurement is developed and validated in "modeling the 10-junction PPC." The optoelectronic operations of multi-junction PPCs are studied with a

Please cite this article in press as: Forcade et al., Multi-junction laser power converters exceeding 50% efficiency in the short wavelength infrared, Cell Reports Physical Science (2025), https://doi.org/10.1016/j.xcrp.2025.102610

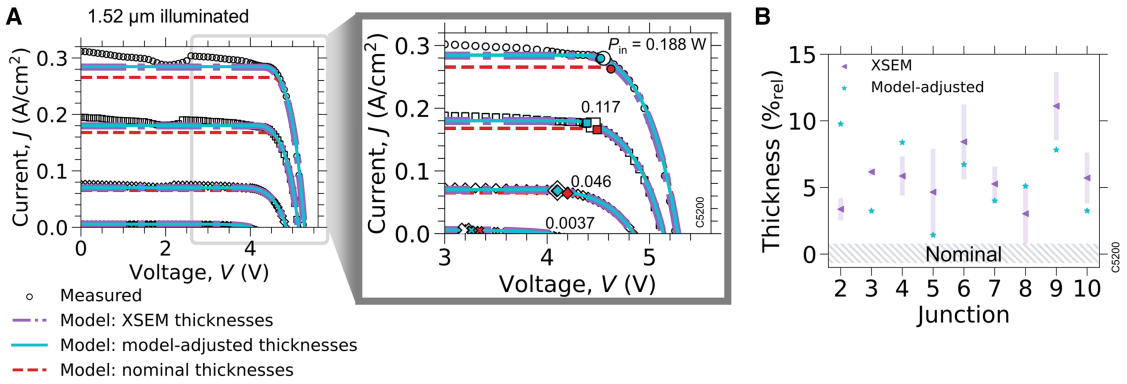

Figure 2. 10-junction InGaAs PPC characterization and model calibration

(A) Comparing current-density-voltage (*J-V*) characteristics of a 1.52-μm laser-illuminated PPC with varying input powers. We include measurements (white symbols) and simulation results that assume cross-sectional scanning electron microscope images (XSEM) thicknesses (dot/dash-purple), model-adjusted thicknesses (solid-blue), and nominal thicknesses (dashed-red). (Right) Zoom in on the *J-V* curves with maximum power point highlighted with large color-coded symbols. The simulated *J-V* curves from XSEM and model-adjusted thicknesses are on top of each other.

(B) Comparing junctions' absorber layer thicknesses relative to nominal targets with values obtained from XSEM and the reverse-bias method (model-adjusted). Note that the XSEM measurement uncertainty generally increases with junction number as the absorber gets thinner. The error bars represent the standard deviation of XSEM measurements over four regions. Also, we do not include confidence intervals for the model-adjusted thicknesses.

calibrated model in both "10-junction PPC characterization and performance" and "enhancing performance through layer-thickness-optimized PPC design." The model is subsequently used to explore the absorber bandgap and wavelength design space in "PPCs designed for 1.0-1.6 μm wavelengths," where we find that increasing the absorber bandgap can enhance PPC efficiency. The exploration guides us to design a four-junction PPC with InGaAsP (bandgap 0.8 eV) absorber layers. We fabricate devices achieving 53.6% efficiency for this material system in the optical fiber transmission window. These results are presented in "high-efficiency four-junction PPC."

RESULTS

10-junction InGaAs PPC

Ten-junction PPCs were grown by metal-organic vapor phase epitaxy (MOVPE) and fabricated at Fraunhofer ISE. A top-down view photo of these devices is shown in Figure 1C and the schematic structure in Figure 1D. The absorber layers of our fabricated 10-junction devices are $In_{0.53}Ga_{0.47}As$ and the bottom junction is denoted as J_1, as labeled in Figure 1D. Single-junction isotypes were also fabricated for model calibration purposes.[34] Model calibration with the 10-junction devices is presented in the main manuscript, while model calibration with the single-junction devices is detailed in Note S1. Further details on the fabrication process can be found in "PPC fabrication."

Our 10-junction PPCs were designed to absorb an equal number of photons in each junction at 1.55 μm when assuming Beer-Lambert absorption with an absorption coefficient of 0.97 μm^{-1} and a cumulative thickness to absorb 97% of the semiconductor-impinging light. The 10-junction device was processed before acquiring the 1.55-μm laser, which lased at a measured 1.52 μm. The 30-nm discrepancy between the nominal and actual laser wavelength highlights the importance of considering laser wavelength variation during PPC optimization. Furthermore, the absorption coefficient used for designing the 10-junction device was 37% larger than the value later measured from the single-junction isotypes for the targeted 1.55-μm wavelength. This difference was not due to the 30-nm wavelength shift and was the dominating factor in lowering the 10-junction PPC efficiency. The measured absorption coefficients are obtained by fitting the Beer-Lambert model to measured internal quantum efficiencies of semi-transparent single-junction isotypes with known absorber layer thicknesses. Further details on our method of obtaining absorption coefficients are provided in "optical properties of materials."

A schematic of the experimental setup is shown in Figure 1E. The laser beam is optionally attenuated with neutral density (ND) filters and then focused such that the light spot is within the PPC's active area. The input power is measured by replacing the PPC with a calibrated thermopile, which captures all the input power due to its two orders of magnitude larger area. Further details on the setup and the power calibration procedure are presented in "optoelectronic measurements" and "calibrated input power."

Modeling the 10-junction PPC

We compare measured and simulated current-voltage curves of the 10-junction PPCs under high-powered 1.52-μm laser illumination with results shown in Figure 2A. We use a 1D model coupling drift-diffusion theory and rigorous coupled wave analysis (RCWA),[35,36] while accounting for luminescent coupling to simulate the optoelectronic properties of the PPC.[30] Our model employs a uniform normally incident radiation and assumes a 3% gridline shading, considering the gridline design of the fabricated devices. This gridline configuration was optimized to minimize the competing lateral resistance and shading losses, based on the anticipated current densities under high illumination. The model also includes a 0.01 Ω resistor in series with the device to account for metallic and lateral resistive losses, as observed in current-voltage curves of single-junction devices. Our model employs physically based parameters from literature, with the

Please cite this article in press as: Forcade et al., Multi-junction laser power converters exceeding 50% efficiency in the short wavelength infrared, Cell Reports Physical Science (2025), https://doi.org/10.1016/j.xcrp.2025.102610

only free parameter being the Shockley-Read-Hall lifetime (τ_{SRH}), a parameter that reflects the bulk crystal and sidewall quality in 1D models. We assume that all absorber layers have the same τ_{SRH}.

The model failed to simultaneously match the measured maximum power point and open-circuit voltage for any value of τ_{SRH} when using growth-targeted layer thicknesses (nominal thicknesses). Simulations either overestimate the open-circuit voltage or underestimate the maximum power point. To accurately model the 10-junction PPC, absorber layer thicknesses must be known precisely, with less than 5% error.

We obtain the thicknesses of the device in two ways: comparing optical simulations with an illuminated reverse-bias measurement (model-adjusted thicknesses) and analyzing cross-sectional scanning electron microscopy images of cleaved samples (XSEM thicknesses). The model-adjusted thicknesses are acquired by illuminating the multi-junction PPC with an absorption mismatching wavelength and measuring the current-voltage curve to far reverse bias, revealing distinct steps. Each step corresponds to the photocurrent of a junction. By aligning the current values from the steps to the modeled photocurrents, individual layer thickness can be deduced. The method can be easily and non-destructively applied to other devices. Conversely, the XSEM method requires destroying the PPCs by cleaving them to obtain cross-sectional images, which are then analyzed to measure the layer thicknesses. Both procedures are detailed in "methods."

We compare absorber layer thicknesses acquired with each method to their nominal thicknesses in Figure 2B. Both methods indicate that absorber layers were thicker than the target, with a mean absolute deviation of the layer thicknesses from the target of 5% for the model-adjusted thicknesses and 6% for the XSEM thicknesses. This 5%–6% deviation from the target was caused by a growth-rate drift in the epitaxy reactor relative to its calibration. The mean absolute difference between the thicknesses obtained from either method is 2.9% and could originate from performing the methods at different locations on the wafer. However, Figure 2A shows that simulated current-voltage curves using the same τ_{SRH} and either the reverse-bias or XSEM thicknesses are indistinguishable from each other but different from those that would have been produced by a device with nominal thicknesses. For example, the simulated short-circuit currents are within 0.1% of each other, but are 8% smaller for the device with nominal thicknesses. These results validate our reverse-bias method.

We find that a τ_{SRH} of 0.11 μs gives the best agreement between the measured and simulated current-voltage curves across the 0.06–3 W/cm^2 irradiance range with 1.52 μm wavelength, the results are shown in Figure 2A. Our τ_{SRH} is shorter than those in Gfroerer et al. and Walker and Denhoff,[37,38] which ranged from 1.7–2.6 μs as well as the single-junction isotype cells that showed 3 μs from fitting the dark current-voltage measurements (single-junction results are presented in Note S1); this reduced lifetime could be caused by the additional thermal load on the epi-material arising from the overall 6.2 times longer growth time for the 10-junction device. Our model predicts the measured maximum power point within <1% across the illumination range explored.

The simulated current-voltage curves fail to align with measurements near short-circuit (J_{sc}) due to the omission of reverse breakdown, Franz-Keldysh, and quantum-confined Stark effects.[39,40] These omissions do not impact the results presented in this paper, as we focus solely on voltages near maximum power, where no junctions are operating in a breakdown regime. Near short-circuit conditions, the current-limiting junction can operate in reverse breakdown when the other nine junctions operate in forward bias. It is worth noting that the model overestimates the open-circuit voltage (V_{oc}) by 0.4% for a 0.188-W input power (2.94 W/cm^2), which we attribute to cell heating during measurement.

10-junction PPC characterization and performance

We measure our 10-junction PPC under 1.52 μm laser illumination and observe a maximum efficiency of 46.4% ± 1.1% at an irradiance of 35 W/cm^2, a voltage output at maximum power of 5.01 V, and an open-circuit voltage of 5.78 V. The measured open-circuit voltage and efficiency as a function of irradiance are shown in Figure 3A (top) and (bottom), respectively. We also include calculated values from our validated model and the radiative limit for the device structure. We obtain a good agreement between the validated model, which uses the model-adjusted thicknesses and τ_{SRH} of 0.11 μs, and the measurements for average irradiances up to 10 W/cm^2. The deviation above 10 W/cm^2 is due to cell heating and lateral series resistance,[22] which our model does not account for. The measured V_{oc} was up to 0.4 V lower than the simulated voltage at an irradiance of 50 W/cm^2, corresponding to an average 0.04 V drop per junction. This voltage reduction is similar to the 0.035-V heating-induced drop of the single-junction GaAs PPC from Geisz et al.[41] when illuminated with the same intensity. The radiative limit is calculated with the detailed balance model presented in Xia and Krich,[26] assuming no reflection losses and 98% absorption. The measured efficiency approaches the radiative limit as irradiance increases, with a minimum difference of 27%$_{rel}$ at 10 W/cm^2.

To improve the performance of our 10-junction PPC, we use our model to determine how it loses efficiency. We simulate the current collection and loss mechanisms normalized to the maximum achievable current from the photon flux at 10 W/cm^2 irradiance, with results shown in Figure 3B (top). The device collects at most 78% of the potential current density (J), with the remainder going to optical and recombination losses. The optical losses include a 5% transmission loss into the substrate, a 3% reflection loss from the antireflection coating (which was optimized for a 1.55 μm wavelength) along with 3% gridline shading.

We can see the effects of the current mismatch between the junctions by segregating the device's current generation and loss mechanisms in each junction at the maximum power point when illuminated with 10 W/cm^2, shown in Figure 3C (top). At 1.52 μm, the fabricated design absorbs 37% more light (J_{ph}) in the bottom junction than in the top junction. This current mismatch occurred due to designing the PPC with an over-estimated absorption coefficient and is not attributable to the 30-nm shift in the operational vs. targeted wavelength. Figure 3C shows that the bottom junctions (J_1–J_3) radiate significantly (J_{rad}) due to the overproduction of current and reabsorbs much of that

Please cite this article in press as: Forcade et al., Multi-junction laser power converters exceeding 50% efficiency in the short wavelength infrared, Cell Reports Physical Science (2025), https://doi.org/10.1016/j.xcrp.2025.102610

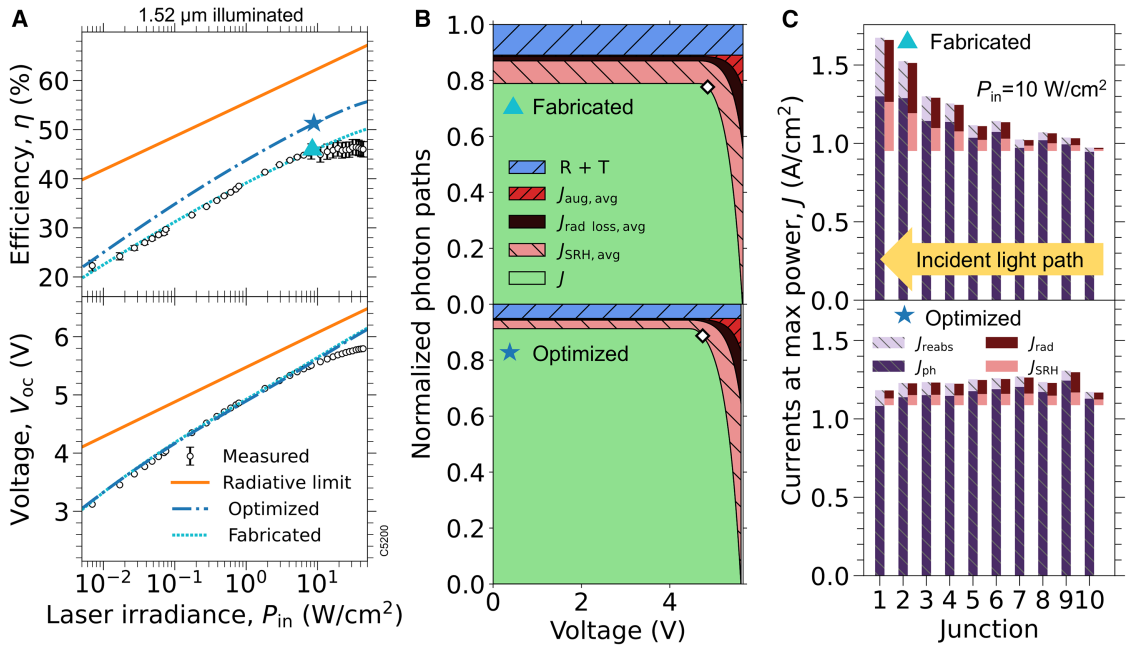

Figure 3. 10-junction InGaAs PPC performance

(A) Efficiency (top) and open-circuit voltage (bottom) vs. 1.52 μm laser irradiance, comparing calibrated measurements with simulation (short-dash). The plots also include the performances of the layer-thickness-optimized design (long-dash) and the radiative limit (solid). The error bars are calculated by propagation of error from the uncertainty in the measurements.

(B) The stack plots depict the extracted current (J) and loss mechanisms averaged over all the junctions, normalized to the incident photon flux, of the fabricated (top) and optimized (bottom) PPC designs illuminated with a 1.52-μm laser at 10 W/cm^2. The white diamond highlights the maximum power point.

(C) Bar charts separating current generation and recombination in each junction at the maximum power point of the fabricated (top) and optimized (bottom) PPC designs illuminated with a 1.52-μm laser at 10 W/cm^2. The yellow arrow indicates that the light is incident on J_{10}. (B and C) The currents include reabsorbed photons (J_{reabs}), first-pass photon absorption (J_{ph}), first-pass photon loss from reflection at the top surface and transmission into the substrate (R + T), SRH recombination (J_{SRH}), Auger recombination (J_{aug}), radiative recombination (J_{rad}), and photons from radiative recombination that escape into the substrate or outside the top of the cell ($J_{rad\ loss}$). Note that the thinnest top junction is J_{10} and currents with an "avg" subscript are the averaged currents over all junctions.

radiation (J_{reabs}) due to their thicker nature, with less luminescent coupling to the top junctions, which produce the least photocurrent. Although J_{sc} increased by 2.2% due to luminescent coupling in this device, excess absorption in the bottom junction causes approximately half of the radiative recombination to escape to the substrate. Redesigning the cell to have matched J_{ph} minimizes these losses, as outlined in the optimized device shown in Figure 3C (bottom).

Enhancing performance through layer-thickness-optimized PPC design

Despite achieving high efficiencies, we sought to understand how our 10-junction PPC could better perform with more ideal absorber layer thicknesses. We optimize its performance assuming the same material quality (τ_{SRH} of 0.11 μs). The optimized PPC design employs luminescent coupling-optimized absorber layer thicknesses calculated using the detailed balance model.[26] We use the detailed balance model instead of our drift-diffusion model for optimization due to its four orders of magnitude lower computational cost, despite its limitations, such as neglecting optical interference between layers and assuming infinite carrier mobilities. Refer to "layer-thickness-optimized design" for more details on the optimization method. Our simulations indicate that this layer-thickness-optimized design achieves up to a 0.25%$_{rel}$ increase in efficiency and up to a 0.2% increase in the maximum power point voltage compared with an identical InGaAs 10-junction design with simple absorption-matched layer thicknesses calculated using rigorous coupled wave analysis. The Note S4 has more details on this performance comparison.

The performance of the layer-thickness-optimized 10-junction PPC is shown in Figure 3A labeled "Optimized" for a 1.52-μm laser illumination. The optimized device efficiency is 19%$_{rel}$ less than the radiative limit but 15%$_{rel}$ more than the fabricated PPC design with minimal impact on V_{oc}.

The optimized device is designed to trap photons from radiative recombination. It exploits a configuration with current-limiting top (J_{10}) and bottom junctions (J_1), as shown in Figure 3C (bottom), and has its highest photogenerated current at junction 9 (J_9). This design is optimal since fewer than 10% of emitted photons can escape through the top due to total internal reflection and photons emitted toward the substrate are mostly reabsorbed by the accumulated thickness of the underlying layers. The simulated current-voltage curve shown in Figure 3B (bottom) reveals that these changes reduce the escape probability of radiative photons ($J_{rad\ loss,avg}$) by 81%$_{rel}$ and improve the J_{sc} gain from luminescent coupling by 50%$_{rel}$, both relative to the fabricated design.

Please cite this article in press as: Forcade et al., Multi-junction laser power converters exceeding 50% efficiency in the short wavelength infrared, Cell Reports Physical Science (2025), https://doi.org/10.1016/j.xcrp.2025.102610

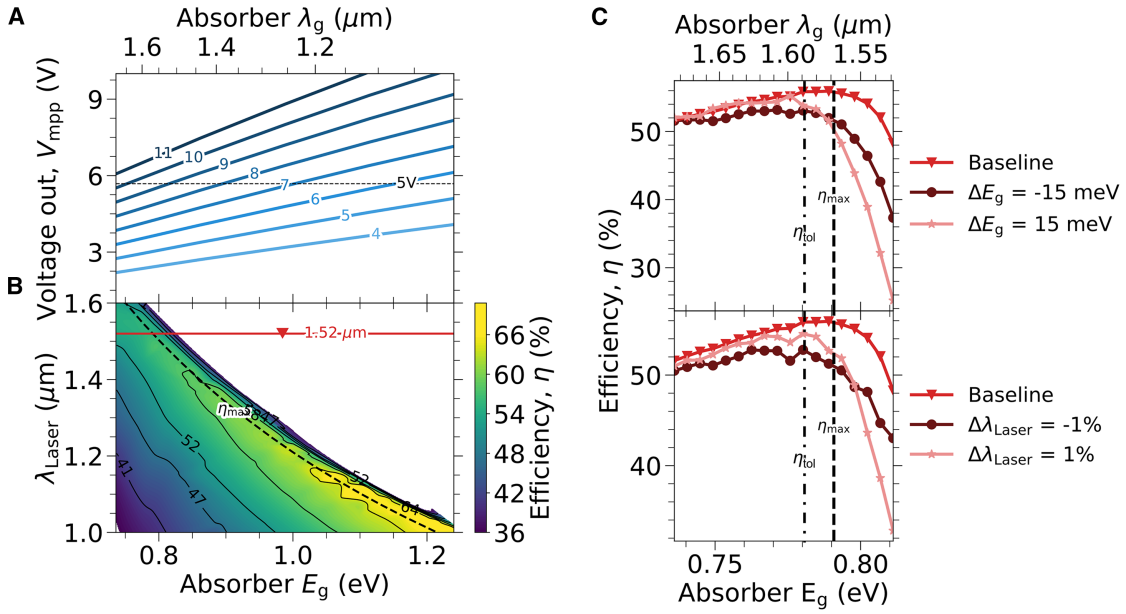

Figure 4. Multi-junction PPCs designed for 1- to 1.6-μm laser wavelengths

(A) Maximum power point voltage of four- to 11-junction InGaAsP PPCs as a function of absorber bandgap. We employ laser photon energies that are 0.03 eV larger than the absorber bandgap. The horizontal dashed line indicates the 5-V threshold.

(B) Efficiency as a function of layer-thickness-optimized devices' laser wavelength and absorber bandgap. The dashed line follows the maximum efficiency (η_{max}) designs attained for each laser wavelength.

(C) Sensitivity analysis of the efficiency for PPCs optimized for each absorber bandgap and 1.52-μm laser wavelength. Presenting the impact of varying, (top) the absorber bandgap (ΔE_g) and (bottom) the laser wavelength ($\Delta\lambda_{Laser}$), on the baseline system. We highlight the more tolerant device to sub-optimal scenarios (η_{tol}), designed with a photon energy offset of 35 meV from the bandgap. In all panels, the laser irradiance is 10 W/cm^2 and τ_{SRH} = 0.11 μs.

The optimized design exhibits a higher extracted current (J) owing to increased light absorption and reduced recombination losses. The sum of the absorber layer thicknesses of the optimized design is 32% thicker than that of the fabricated design, resulting in 3% less transmission loss into the substrate. However, achieving these thicker layers necessitates longer growth times, which could impact device performance by reducing carrier lifetimes but was not modeled. Antireflection coating optimization for 1.52-μm light eliminates a further 3% reflection loss. The optimized design has a lower recombination loss for the same τ_{SRH} due to a more uniform distribution of current generation among the junctions. The SRH recombination ($J_{SRH,avg}$) loss near J_{sc}, shown in Figure 3B (top) is more than double for the fabricated device at 8% vs. 3% for the optimized device.

In case material can be grown with higher quality, we also explore the impact of improving τ_{SRH} from 0.11 μs to 3 μs on the optimized multi-junction PPC performance. We generate a layer-thickness-optimized design and simulate an efficiency of 57% for a 1.52 μm wavelength irradiance of 10 W/cm^2. This efficiency is 0.75%$_{rel}$ above an absorption-matched design, 10%$_{rel}$ above the layer-thickness-optimized design with τ_{SRH} of 0.11 μs, and only 9%$_{rel}$ below the radiative limit.

PPCs designed for 1.0- to 1.6-μm wavelengths

We explore the flexibility and potential of a layer-thickness-optimized PPC design for the 1.0- to 1.6-μm wavelength range with 10 W/cm^2 irradiance. We consider multi-junction devices with the same metallic grid and layer structure as our fabricated devices with InGaAsP absorbers lattice-matched to InP, assuming identical quaternary composition for all junctions. Bandgap, electron affinity, permittivity, carrier mobilities, and carrier effective masses for InGaAsP were interpolated from InGaAs to InP based on recommendations from the literature.[21,42–44] The complex refractive index was interpolated between endpoints with the morphing algorithm from Schygulla et al.[45] Details on the interpolation schemes can be found in "optoelectronic model" and "optical properties of materials." We report the bandgap of the material based on the simulated quantum efficiency of a single-junction isotype with 4-μm-thick absorber layers, using the method from Helmers et al.[46] We use layer-thickness-optimized designs, with a τ_{SRH} of 0.11 μs. We determine the number of junctions required to achieve an operating voltage larger than 5 V by simulating the current-density-voltage characteristics as a function of the absorber bandgap; this is illustrated in Figure 4A. This simulation employs input photon energy 30 meV larger than the bandgap, for four to 11 junctions, with each variation using a new optimized PPC design. We show the intersections with 5 V in Figure 4A. The function used to relate the voltage to the bandgap is provided in the Note S5.

Using the minimum number of junctions obtained from Figure 4A to ensure the operating voltage of each device is at least 5 V, we evaluate the efficiency of optimized devices as a function of laser wavelength and absorber bandgap (see Figure 4B). We observe no discontinuity arising from changes

in the number of junctions, which agrees with the results from Algora et al.[2] that predicted a flat efficiency profile for PPCs with five or more junctions and output powers around 10 W/cm^2. The black dashed curve in Figure 4B shows the maximum efficiency (η_{max}) for all laser wavelengths and occurs at photon energies 25 meV larger than the absorber bandgap over the investigated range. This offset varies from the value of 87 meV found by Höhn et al.[25] for single-junction GaAs PPCs. Their absorber was only 3 μm thick compared with our 7 μm, so closer-to-bandgap photon energies suffered from large transmission losses for the thin absorber. Following the dashed curve in Figure 4B also reveals that efficiency increases from 53% to 67% as the absorber bandgap increases and that there is a steep drop-off as wavelength approaches the absorber bandgap. The efficiency increases with larger absorber bandgaps due to the improving bandgap-voltage offset.

We varied the absorber bandgap and the laser wavelength in simulations to gauge the sensitivity of optimized devices in sub-optimal scenarios. The results are depicted in Figure 4C, where the baseline shows the optimized systems, and the other curves are perturbations to the systems without re-optimization of the structure. The results shown are for optimized PPC structures at a laser wavelength of 1.52 μm. Similar behavior was simulated for optimized PPC structures at 1.06-μm and 1.31-μm laser wavelengths. We vary the bandgap by ±15 meV as it corresponds to a reasonable target range, assuming no significant temperature drift during long epi-growths. We vary the wavelength by ±1% (±15 nm), corresponding to the room temperature wavelength range observed over the output powers for the 1.52-μm laser used in the experiments.

Our sensitivity analysis suggests a better compromise between maximum achievable efficiency and system tolerance when designing PPCs using a larger offset between the photon energy and bandgap. For example, designing with an offset of 35 meV (η_{tol}, vertical dot-dashed line in Figure 4C) lowers the baseline efficiency by 0.2%$_{rel}$ compared with the design with a 25 meV offset (η_{max}, vertical dashed line in Figure 4C) but can operate at efficiencies up to 3%$_{rel}$ higher for sub-optimal scenarios of ±1% laser shift or ±15 meV bandgap shift. In either case, positive wavelength and bandgap shifts (light red curves in Figure 4C) are preferable to negative shifts (dark red curves in Figure 4C) for the η_{tol} design, resulting in up to 3.2%$_{rel}$ higher efficiencies. These higher efficiencies appear to be due to a smaller absorption mismatch from positive shifts compared with negative shifts.

High-efficiency four-junction PPC

Results from the previous section demonstrate that a higher absorber bandgap promises higher PPC efficiencies while also requiring fewer junctions. However, long-haul power-by-light systems require laser wavelengths longer than 1.45 μm to minimize optical attenuation within fibers (Figure 1B). Therefore, using our model, we designed a four-junction PPC targeting lattice-matched InGaAsP absorber material with a bandgap of 0.8 eV for 1.48-μm laser illumination. The design offers a large fabrication and system tolerance with a 38-meV offset between photon energy and bandgap to minimize thermalization losses. Although nine junctions are required to reach the 5 V threshold, we opted for four junctions as a compromise between minimizing fabrication risk, showcasing the predictability of our model, and supporting our argument that larger bandgap absorbers improve PPC efficiency. The PPC design was optimized using our calibrated optical coefficients and includes an optimized antireflection coating, absorber layer thicknesses that are absorption-matched based on Beer-Lambert absorption, and a cumulative absorber thickness that absorbs 98% of the light. We chose Beer-Lambert thicknesses over layer-thickness-optimized thicknesses to maintain consistency with the fabricated 10-junction devices.

We measure current-voltage characteristics of the four-junction PPC under 1.446-μm laser illumination and observe an average efficiency of 53.3% at an irradiance of 15.1 W/cm^2 with a standard deviation of 0.3%$_{abs}$ over 10 randomly selected devices spread across a quarter of one substrate, from center to edge (the Note S6 plots this and other performance metrics for the 10 devices). The best device had a maximum efficiency of 53.6% ± 1.3% at an irradiance of 15.2 W/cm^2 and a voltage output at maximum power of 2.18 V; this result is shown in Figure 5A. The PPC was fabricated before the laser was acquired, which is why the 1.48-μm wavelength design target differs from the measurement wavelength of 1.446 μm.

The measurement is compared with simulation in Figure 5A, using our model with nominal layer thicknesses and a τ_{SRH} of 0.4 μs which best fit the measurement. The growth rate was carefully calibrated for this device, leading to increased confidence in the nominal thicknesses. The τ_{SRH} of 0.4 μs is over three times longer than in the 10-junction InGaAs-based PPC but still an order of magnitude shorter than in the single-junction InGaAs isotypes, possibly due to the growths' thermal budget difference from different growth durations. The growth time for the four-junction devices was 4.4 times longer than that of single-junction devices, yet 30% shorter than that of 10-junction PPCs. The measured and simulated data in Figure 5A overlap within incident power uncertainty, except at open-circuit voltage. At open-circuit voltage, the discrepancy with simulations of about 0.01 V per junction is attributed to device heating, which is not accounted for in the model. This voltage reduction agrees with the 0.01 V heating-induced drop of the single-junction GaAs PPC from Geisz et al.[41] when illuminated with the same intensity.

The efficiency as a function of irradiance is shown in Figure 5B, where we compare measurements to simulations with τ_{SRH} of 0.4 μs. The validated model aligns well with the irradiance measurements between 1 and 20 W/cm^2. We attribute the deviation above 20 W/cm^2 to cell heating and series resistance, following our previous work of single-junction PPCs using similar metallizations.[22] The deviation below 1 W/cm^2 could be attributed to devices with a very resistive path to a high recombination center[47] or a carrier concentration-dependent bulk SRH recombination.[32,48,49] The behavior is evident by the appearance of a hump in the dark current-voltage curve as shown in Figure 5C, emphasized by the shaded gray area named transition zone. We correlate the transition zone to the maximum power point voltages and then relate it to the laser irradiances in Figure 5D. This zone corresponds to the region in Figure 5B, where the measured efficiencies lie between simulated curves that assume a τ_{SRH} of 0.07 μs and 0.4 μs. The measured hysteresis in the

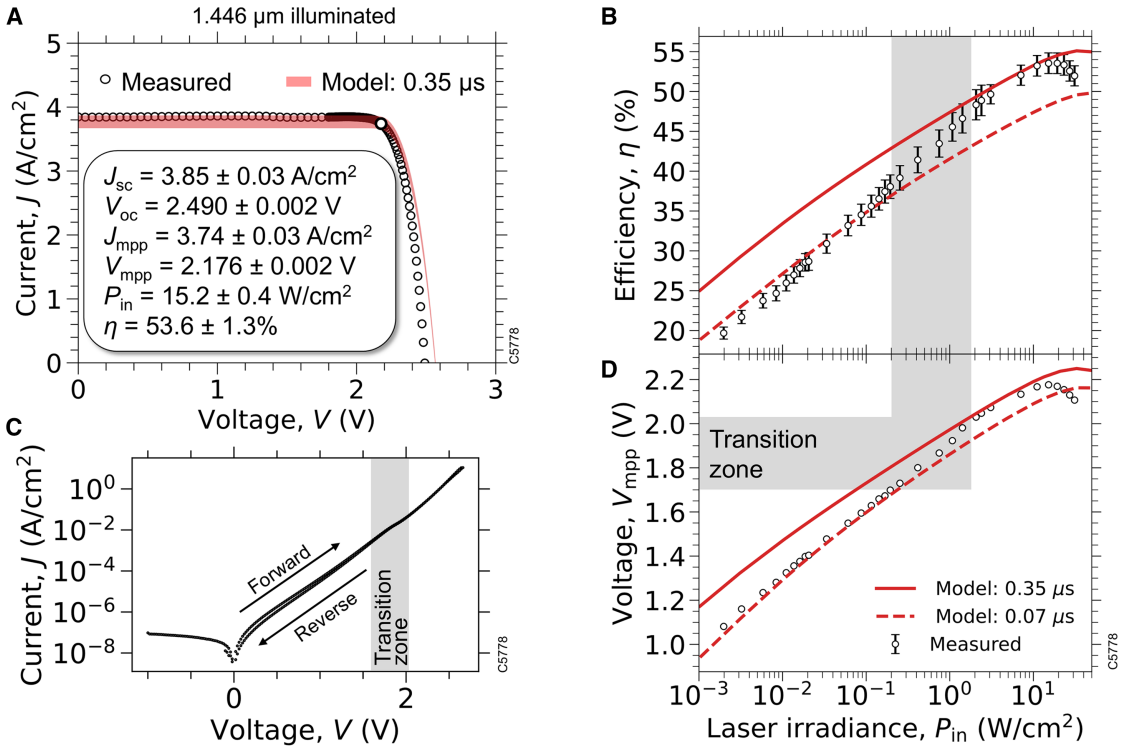

Figure 5. Four-junction InGaAsP PPC performance

(A) Current-density-voltage (*J-V*) characteristics of a 1.446-μm laser-illuminated PPC operating at its highest efficiency at an irradiance of 15.2 W/cm^2. Comparing to simulations with τ_{SRH} of 0.4 μs, the red-shaded region spans the measured input power uncertainty.

(B) Efficiency vs. 1.446-μm laser irradiance, comparing calibrated measurements to simulations with τ_{SRH} of 0.4 μs and 0.07 μs. The error bars are calculated by propagation of error from the uncertainty in the measurements.

(C) Measured dark current-density-voltage curve of the high-efficiency PPC, including a forward (top data points) and reverse voltage sweep. The shaded area named "transition zone" highlights the voltages near the hump in the curve.

(D) Measured voltages at the maximum power point as a function of 1.446-μm laser irradiance. The voltages within the "transition zone" from (C) are highlighted here and the shaded area is extrapolated along the laser irradiance values that intersect the "transition zone." All simulations use nominal thicknesses.

low-voltage region of the dark current-voltage curve shown in Figure 5C suggests the presence of a trap saturation mechanism, supporting our claim of carrier concentration-dependent bulk SRH recombination.

Our model predicts the four-junction PPC will achieve an efficiency of 56% at an irradiance of 15.2 W/cm^2 when illuminated by its intended laser wavelength of 1.48 μm. The 4.7%$_{rel}$ drop in efficiency from using a 2.4% shorter laser wavelength demonstrates the PPC's robustness to laser wavelength variation.

DISCUSSION

Our work paves the way for integrating PPCs into telecommunication and free space power-by-light systems due to the transmission windows in the 1.0- to 1.6-μm wavelength range within fibers and the earth's atmosphere.[1,2] We presented four significant outcomes.

(1) We propose and validate a method that accurately estimates the thicknesses of absorber layers for multi-junction devices using a single non-destructive measurement combined with accurate modeling. This method presents a promising avenue for estimating absorber layer bandgaps and thicknesses simultaneously, in multi-junction devices. By employing several illumination wavelengths equal to one plus the number of junctions and leveraging known absorption coefficient data as a function of bandgap, absorber bandgaps and layer thicknesses can be iteratively adjusted in the optical model until simulated photogenerated currents align with experimental measurements.

(2) We develop a model that accurately predicts PPC performance. This predictive model can be further enhanced by integrating machine learning methods[50] for PPC design optimization. On top of efficiency enhancements, a trained algorithm could refine PPC optimization across various figures of merit, such as minimizing epitaxial growth times through thinner designs or developing more fabrication-tolerant structures.

(3) We introduce a PPC design optimization process leveraging a computationally efficient method to include luminescent coupling effects, predicting higher efficiencies and output voltages than a simple absorption-matched design.

(4) We demonstrate that >50% PPC efficiencies are achievable when operating at room temperature in the transparent window of optical fibers through careful design optimization using a calibrated model combined with precise epitaxial growth, as evidenced by our four-junction InGaAsP PPC optical-to-electrical efficiency of 53.6% ± 1.3% for a 1.446-μm laser wavelength and 15.2 W/cm^2 irradiance.

We also report on realizable PPC efficiencies over the critical laser wavelength range of 1.0–1.6 μm. Within this range, our validated optoelectronic model predicts efficiencies of up to 67% for InGaAsP PPCs. The model suggests that the efficiency of PPCs increases with absorber layer bandgap. These findings will serve as a valuable guide for future telecommunication system optimizations to maximize efficiency over various fiber transmission lengths. For example, if the electrical-to-optical laser efficiencies are the same for 0.82-μm and 1.6-μm wavelengths and PPC efficiencies are 65%[14] and 52%, respectively, the longer-wavelength system exhibits a higher efficiency for travel distances exceeding 0.43 km within optical fibers (assuming attenuation from Figure 1B). Given the input power limits of optical fibers,[8] we can reduce the quantity and diameter of fibers required for long-haul (>1 km) power-by-light applications with more efficient PPCs in the 1.0- to 1.6-μm range.

The multi-junction PPC designs investigated in this work have further opportunities for technical improvements. One pathway forward is to use transparent front contacts,[51] which could improve our device's efficiency by 3%$_{rel}$. Another strategy is to enhance heat dissipation with device packaging (required for commercialization, ex: thermal paste) and/or substrate removal (difficult to manufacture and design). Geisz et al.[41] demonstrated that unpackaged illuminated GaAs PPCs on substrates at ~30 W/cm^2 (irradiance near our maximum measured efficiency) had an efficiency loss due to temperature of 5%$_{rel}$, which approaches the difference between our simulation and measurement of 5.6%$_{rel}$ for the fabricated 10-junction device shown in Figure 3A; comparatively, thin films released from the growth substrates had a negligible loss. Replacing the substrate with light trapping structures can also enable a 10%$_{rel}$ efficiency gain[52,53] by reducing SRH recombination through 10 times reduced cumulative absorber thickness and reducing radiative loss out of the device. A thinner device reduces epitaxy-related costs and could improve crystal quality if the thermal load is responsible for the shorter τ_{SRH} observed in the multi-junction PPCs compared with single-junction PPCs. However, a back-reflector design can increase post-growth fabrication costs, lower device yield,[54] and requires careful layer-thickness optimization.

METHODS

PPC fabrication

Ten-junction InGaAs PPCs and four-junction InGaAsP PPCs grown lattice-matched on a p-type InP substrate were fabricated at Fraunhofer Institute for Solar Energy Systems. Employing metal-organic vapor phase epitaxy (MOVPE) on an Aixtron G4 2800TM reactor, the epitaxial layer structures were grown on 4-inch InP wafers. More details regarding the epitaxy process can be found elsewhere.[55] All junctions were grown with tunnel diodes between each junction within one growth run. The junctions have either $In_{0.53}Ga_{0.47}As$ or InGaAsP absorber layers lattice-matched to InP and cladded between larger bandgap front and back surface field (FSF and BSF) layers. The junctions are identical, except for the individual absorber layer thicknesses, the bottommost BSF layer material, and the topmost FSF layer-thickness and doping concentration. The topmost FSF layer was designed as a lateral conduction layer[56] comprising 1,000 nm of $n = 5 \times 10^{18}$ cm^{-3} InP. The absorber layer thickness decreases from the bottom junction (J_1) to the topmost junction (J_{10}/J_4). After completing the epitaxy, ohmic contacts and a Ta_2O_5/MgF_2 antireflection coating were deposited. Individual PPCs on the wafer were isolated using unselective wet-chemical mesa etching. The resulting chip dimensions were 2.2 × 2.9 mm^2, with a nominal mesa area of 0.064 cm^2 and a designated area discounting busbars of 0.054 cm^2. For all densities provided in this work, we divide by the nominal mesa area.

Quantum efficiency and reflectivity measurements

The PPC devices' external quantum efficiency and spectral reflectivity were measured with an Oriel IQE200. The reflectivity measurement only includes perpendicularly reflected light as an integrating sphere was not used for the measurements.

Optoelectronic measurements

The measurement station is illustrated in Figure 1E. The laser light passed through a ~1-m-long multimode fiberoptic cable with a diameter of 400 μm and a 0.22 numerical aperture and then collimated by a lens. The intensity was optionally attenuated with two neutral density (ND) filters, which could be used interchangeably or together to reach a wide range of input powers. The collimated beam was redirected by a mirror and concentrated with a lens onto the PPC device. The working distance between the lens and the PPC was set to achieve under-illumination, i.e., a smaller light spot than the area between the busbars, and to maximize illumination uniformity while providing alignment reproducibility. This follows the procedure outlined in Beattie et al.[22] To measure the incident power on the PPCs, a Newport 919P-030-18 thermopile calibrated on December 8, 2021, with certificate number 3038470-001, was positioned at the PPC location. Each thermopile measurement required at least 30 s to allow for stabilization. The thermophile absorbs all light that would be collimated on the PPCs and more, as it has a 2.27-cm^2 sensor area, two orders of magnitude larger than the PPC device area. The efficiency of the devices was measured by dividing the output power at the maximum power point on the current-voltage curve by the calibrated input power.

The PPCs were vacuum held on a thermoelectric cooled, gold-plated copper chuck with the temperature fixed at 25°C. The current-voltage characteristics (*I-V*) of each photovoltaic device were measured using a Keithley 2420 in a four-wire configuration under laser illumination. Current collecting probes were placed on both busbars. Each light *I-V* measurement was collected within 2 s or more and included a forward and backward sweep. The maximum power output is calculated by averaging the currents from the forward and backward-swept *I-V* curves. We set

Please cite this article in press as: Forcade et al., Multi-junction laser power converters exceeding 50% efficiency in the short wavelength infrared, Cell Reports Physical Science (2025), https://doi.org/10.1016/j.xcrp.2025.102610

the Keithley's number of power line cycles (NPLC) parameter to 1. No device preconditioning was performed. The cells were measured and stored in a laboratory room with a temperature of 21°C–22°C and relative humidity of 30%–40% at one atmospheric pressure. The maximum power point of the illuminated *I-V* measurements was determined with a cubic spline interpolation.

Calibrated input power: 1.52-μm laser

A QPC LASERS 6015-0007 15-W 1.55-μm laser with a nominal lasing wavelength of 1.520 ± 0.002 μm was used. The current to the laser driver was varied over a range of 10–18 A to modify the laser power. The measured 1.52-μm central wavelength varied with the laser's current and operating temperature. To keep lasing at 1.520 ± 0.002 μm, the laser temperature was adjusted. Between measurements with the laser, the beam was blocked in front of the ND filters until the laser temperature stabilized to within 0.05°C of our target.

The unfiltered 1.52-μm laser power was calibrated with the thermopile placed at the PPC's location ($P_{in} > 8$ W/cm^2). According to the calibration spec sheet, the thermopile was 1.001 times more sensitive relative to the calibration wavelength of 1.064 μm for the 1.52 μm wavelength, thus the measured input power was adjusted accordingly. The filtered laser power was calibrated with a three-step process ($P_{in} < 8$ W/cm^2). First, using the thermopile placed at the PPC's location in Figure 1E, the incident power ($P_{in,th}$) as a function of the drive current in the absence of ND attenuators was measured. Next, the short-circuit current (I_{sc}) of single-junction isotypes with 60-nm and 180-nm absorber layer thicknesses at the same laser driver currents was directly measured. Data showing device heating effects were filtered out to ensure a linear relationship between I_{sc} and $P_{in,th}$ was obtained. Using these datasets that do not include ND filters, the spectral response (*SR*) was extracted by fitting to $I_{sc} = SR \times P_{in,th}$. The fits followed the data closely with minimal scatter. The *SR* values for the 60-nm and 180-nm isotypes averaged over four devices for each thickness were 0.04857 ± 0.00009 A/W and 0.1259 ± 0.0002 A/W, respectively. The standard deviation for these devices is provided as an uncertainty. The isotypes' I_{sc} for all filter combinations was measured and their input powers ($P_{in,iso}$) were calculated using

$$P_{in,iso} = \frac{I_{sc}}{SR} \quad \text{(Equation 1)}$$

Finally, the average of $P_{in,iso}$ from the eight devices was taken to calculate the calibrated ND-filtered input power (P_{in}).

The incident power dominated the uncertainty of our calibrated measurements. The sources of error for our efficiency measurement included the following:

(1) ±1.9% calibration uncertainty for the thermopile.
(2) Uncertainty on $P_{in,th}$: ±max (0.5 mW, 1.5%) where the first is the power meter precision and the second is from fluctuations in measurement conditions.
(3) Uncertainty on V_{mpp} from the source meter: ±(0.012% + 1.3 mV).
(4) Uncertainty on I_{sc} and I_{mpp} from the source meter:
    - o I < 10 mA: ±(0.035% + 5.6 μA)
    - o 10 mA ≤ I < 100 mA: ±(0.055% + 56 μA)
    - o 100 mA ≤ I < 1 A: ±(0.066% + 1.57 mA)

Calibrated input power: 1.446-μm laser

A BWT KE70HAEFN-7.0W 1.47-μm laser was used with a nominal lasing wavelength of 1.446 μm. The central wavelength varied with the laser's current by ±0.001 μm. We found little change in laser wavelength as a function of laser drive current, compared with the 1.52-μm laser, probably due to better heat dissipation within the laser.

The unfiltered input power ($P_{in} > 3$ W/cm^2) was measured by placing the thermopile at the PPC location. According to the calibration spec sheet, the thermopile was 1.002 times more sensitive relative to the calibration wavelength of 1.064 μm for the 1.446-μm wavelength, thus, the measured input power was adjusted accordingly. Conversely to the 1.52-μm laser, the ND-filtered input powers ($P_{in} < 3$ W/cm^2) were calibrated by applying a multiplicity factor to the filtered input powers such that the overlapping efficiency values matched. The uncertainties to the filtered input powers were propagated accordingly.

Optoelectronic model

The Synopsys TCAD Sentaurus software version S-2021.06 US was used to simulate the PPC devices, employing a one-dimensional drift-diffusion model that treated the devices as laterally infinite layered structures. Through the S4 open-source software[35,36] based on rigorous coupled wave analysis (RCWA), the optical behavior was simulated to enable calculations of the depth-resolved generation rate of electron-hole pairs. Details on material optical properties are provided in the next section. Monochromatic illumination was assumed from the lasers. It was assumed that all transmitted light into the highly p-doped InP substrate was lost due to free-carrier absorption.[57]

To model electrical transport, Poisson's equation coupled with carrier drift and diffusion equations were solved, assuming Fermi statistics, to determine the *J-V* curves as well as depth-resolved recombination rate profiles accounting for radiative, Auger, and Shockley-Read-Hall recombination.[31] Data from the plots generated by Bardyszewski and Yevich[44] were used to relate the Auger coefficient to the InGaAsP composition. The model and parameters provided by Sotoodeh et al.[42] were used to simulate the charge carrier mobilities, assuming equivalent minority and majority carrier mobilities. The mobility parameters from Lumb et al.[43] were used for InAlAs. For the rest of the InGaAsP electrical parameters, the interpolation schemes and values from Vurgaftmann et al.[21] were used. Due to the PPCs' high-quality material, a detailed model of luminescent coupling from Wilkins et al.[30] was used to account for radiative reabsorption in all parts of the device. To correctly model the heterointerfaces, thermionic emission and charge carrier tunneling was used.[31] The tunnel diode was modeled using the structure given in Soresi et al.[58]

Optical properties of materials

Complex refractive indices (*n* and *k*) from literature[59–61] and measurements were used to interpolate[45] the *n* and *k* data from three experimental supporting points $In_{0.53}Ga_{0.47}As$ (0.736 eV) to $In_{0.69}Ga_{0.31}As_{0.67}P_{0.33}$ (0.9 eV) to InP (1.34 eV). Spectroscopic ellipsometry based on J.A. Woolam WVASE32 software was used

Please cite this article in press as: Forcade et al., Multi-junction laser power converters exceeding 50% efficiency in the short wavelength infrared, Cell Reports Physical Science (2025), https://doi.org/10.1016/j.xcrp.2025.102610

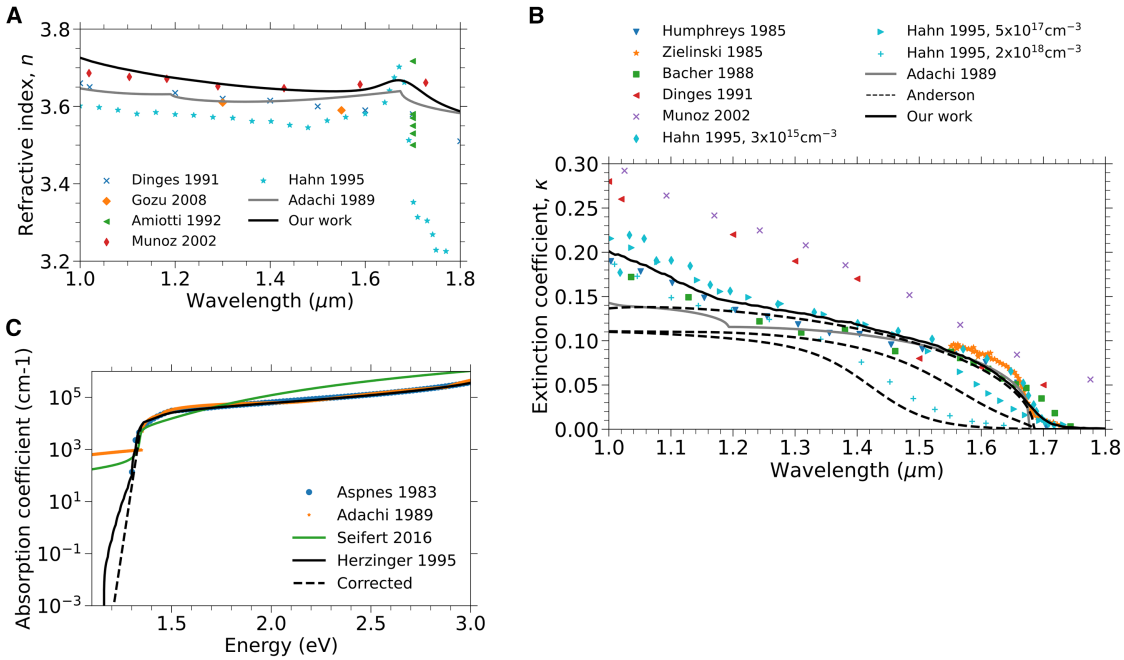

Figure 6. Optical properties of InGaAs and InP

(A) Real part of the refractive index of InGaAs.

(B) Extinction coefficient of InGaAs. We compare our measured values "Our work" with the literature: Adachi,[59] Dinges et al.,[60] Gozu et al.,[64] Amiotti and Landgren,[65] Munoz et al.,[66] Hahn et al.,[63] Humphreys,[67] Zielinski et al.,[68] Bacher et al.,[69] and Anderson.[62] The "Anderson" curves were calculated with matching doping concentrations to the measured data of Hahn et al.: 3×10^{15} cm^{-3}, 5×10^{17} cm^{-3}, 2×10^{18} cm^{-3}.

(C) Absorption coefficient of InP. We compare our corrected data (Corrected) to the literature: Aspnes and Studna,[70] Adachi,[59] Seifert and Runge,[71] and Herzinger et al.[61]

to measure *n*-data for low n-doped InGaAs samples with thicknesses ranging 1–3 μm (Figure 6A). The $In_{0.69}Ga_{0.31}As_{0.67}P_{0.33}$ *n*-data were calculated by interpolating with an initial morph from InGaAs to InP. The *k* of InGaAs and $In_{0.69}Ga_{0.31}As_{0.67}P_{0.33}$ were calculated from external quantum efficiency (*EQE*) and reflectance (*R*) measurements of single-junction isotypes with the respective absorber materials, assuming Beer-Lambert absorption,

$$k = \frac{-\lambda \ln(EQE/(1-R))}{4\pi x} \quad \text{(Equation 2)}$$

where λ is the wavelength of light and *x* is the absorber layer thickness. For the extinction coefficient (*k*) of InGaAs from "Our work," as depicted in Figure 6B, we used a single-junction isotype with a 540-nm-thick low n-doped InGaAs absorbing layer. This method of extracting the extinction coefficient near the band-edge provided a better repeatability between InGaAs thicknesses than using ellipsometry data. For the highly doped n-type absorber layer in the homojunction, carrier-density-dependent *k* was calculated following the model from Anderson[62] due to the strong dependence in InGaAs.[63] We compare our complex refractive indexes with those found in Adachi,[59] Dinges et al.,[60] Herzinger et al.,[61] Gozu et al.,[64] Amiotti and Landgren,[65] Munoz et al.,[66] Hahn et al.,[63] Humphreys,[67] Zielinski et al.,[68] Bacher et al.,[69] Anderson,[62] Aspnes and Studna,[70] and Seifert and Runge[71] in Figure 6.

For smaller bandgap materials such as InGaAs, they have an n-type doping-dependent extinction coefficient due to conduction band filling effects. Hahn et al.[63] measured the n-doping-dependent extinction coefficient for doping concentrations: 3×10^{15} cm^{-3}, 5×10^{17} cm^{-3}, 2×10^{18} cm^{-3}. To generalize to any doping concentration, we use Anderson's model,[62] and compare its results with the measurement of Hahn et al. in Figure 6B, assuming the same doping concentrations.

To improve the interpolation between InGaAs and InP using the morphing algorithm,[45] we modified the InP absorption coefficient at the band-edge from Herzinger et al.[61] and called it "Corrected" in Figure 6C. This modification removes their measured Urbach tail, caused by the Fe-doping of their InP sample. This amendment was achieved by fitting an exponential decay within 1.337–1.342 eV and extrapolating to lower-photon energies. For modeling the optical properties of InP, we employ "Corrected" for the absorption coefficient datasets and the measured real refractive index from Herzinger et al.[61]

Absorber layer thicknesses: Reverse-bias method

To non-destructively extract absorber layer thicknesses, the reverse of the method described by Wang et al.[72] was performed. This method uses fast and simple optical simulations; however, it requires junctions with high shunt resistance, accurate knowledge of the optical properties of the absorber layer, minimal luminescent coupling, and a current-voltage measurement under large reverse-bias under a known illumination

Please cite this article in press as: Forcade et al., Multi-junction laser power converters exceeding 50% efficiency in the short wavelength infrared, Cell Reports Physical Science (2025), https://doi.org/10.1016/j.xcrp.2025.102610

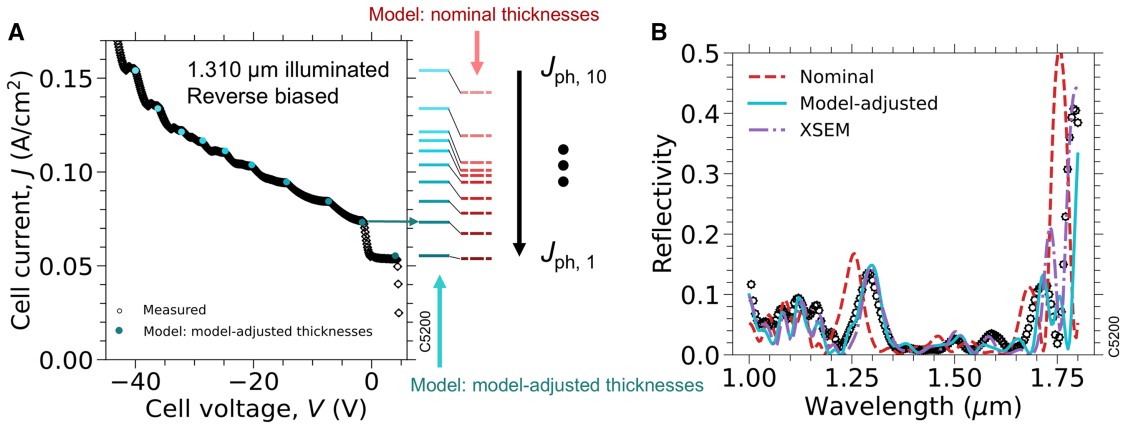

Figure 7. Reverse-bias method for the 10-junction device

Comparing measurement (circles) with simulations that assume growth-targeted thicknesses (dashed-red) and best-fit thicknesses (solid-blue).

(A) Measured current-voltage of the fabricated 10-junction PPC, in far reverse bias, when illuminated with a 1,310-nm laser. The horizontal lines to the right of the plot are the simulated photogenerated currents of each junction, starting with the top (J_{10}) to the bottom (J_1).

(B) Spectral reflectivity of the PPC, also comparing with simulations assuming cross-sectional scanning electron microscope (XSEM) measured thicknesses.

spectrum causing current mismatching. Having extracted the absorption coefficient of the InGaAs absorber material from quantum efficiency measurements of optically thin single-junction isotypes (see previous subsection), we aim to determine the relative absorption of each junction in the 10-junction PPC. The PPC is illuminated with a 1.31-μm laser and the current as a function of voltage is measured from open circuit to a negative bias of −45 V, as shown in Figure 7A. The 1.31-μm laser induces a large current mismatch among all 10 junctions, and the photogenerated current is assumed to monotonically decrease from the top (J_{10}) to the bottom (J_1) junction as they were designed to be current matched at a longer wavelength. As the bias voltage is varied, a phenomenon is observed where the bottom junction (J_1) limits the current until the reverse bias is large enough to put it into reverse breakdown, at which point the current increases up to the new limiting current of the second-from-the-bottom junction (J_2), first step at about –1V seen in Figure 7A.[39,72,73] This process repeats for each junction until the entire device enters breakdown, producing the 10 steps seen in Figure 7A. The sample is illuminated with an irradiance near 0.1 W/cm^2 to minimize the effect of luminescent coupling on the current of each junction.[72] The absence of luminescent coupling is verified in our measurement by observing stable spectral responses for each junction with laser input powers near 0.1 W/cm^2. The Note S2 includes those results. Without luminescent coupling, large junction dark current, and absorption losses, the *J-V* curve's steps correspond to each junction's photogenerated current densities.

Based on nominal thicknesses, the measured and simulated junction photocurrents deviate by up to 10%, as shown to the right of Figure 7A. Therefore, a fit is performed, allowing all junction thicknesses to vary, keeping the thickness ratios between layers within a constant. The photogenerated currents of each junction are fit to the measured steps and the simulated spectral reflectivity is fit to measurement with the results given in Figure 7. To fit the data, the root-mean-square-relative difference between measured and simulated results are calculated for both the photocurrent and the spectral reflectivity. Python's SciPy minimization package with the Nelder-Mead method is used to minimize the sum of those two root-mean-square values. The bottom junction absorbs more than 99% of light reaching it, since a much shorter wavelength is used than what the device was designed for, thus changing its thickness had no impact on the fit. The model-adjusted thicknesses exceeded the targets, with a deviation of up to 10%. We attribute this thickness deviation to a temperature drift during epi-growth. Figure 7B shows that simulated reflectivity assuming the model-adjusted layer thicknesses agrees more closely with the reflectivity measurement than the nominal thicknesses, reducing the root-mean-square-relative-difference from 2.9 to 0.6. We also included simulated reflectivity assuming the XSEM thicknesses (discussion on these thicknesses is provided in the next subsection), which follow the model-adjusted and measurements closely.

Absorber layer thicknesses: XSEM method

To validate the values determined with the reverse-bias method, the thicknesses of individual absorber layers were determined via cross-sectional scanning electron microscope (XSEM) measurements using a Hitachi model SU-70 scanning electron microscope equipped with a back-scattered electron (BSE) detector. Devices were cleaved from the processed wafer and arranged in vise holders, allowing imaging perpendicular to the cleaving plane, and ensuring proper mechanical stability and charge dissipation. The acceleration voltage was kept constant at 10 keV and the working distance as well as the sample stage configurations were optimized to boost the BSE signal contrast and reduce misalignment errors. An exemplary cross-sectional picture of the 10-junction device is shown in Figure 8. To accurately determine absorber layer thicknesses, cross-sectional images of individual junctions were acquired with a magnification up to 110,000×, achieving a resolution of 1.1 nm/pixel. The

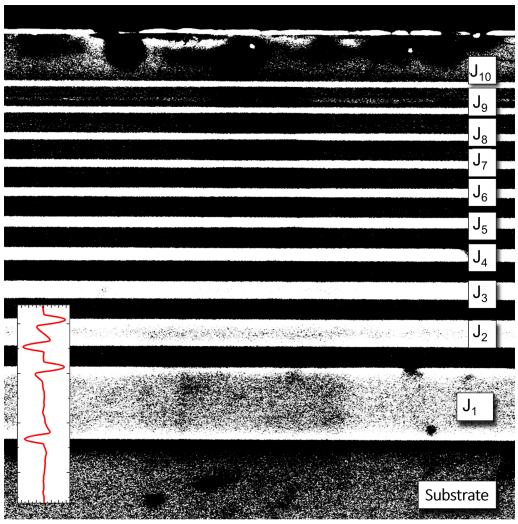

Figure 8. High-contrast cross-sectional SEM image of the 10-junction PPC

The bright areas are the $In_{0.53}Ga_{0.47}As$ absorber layers, whereas the dark areas are the barrier/interlayers of each junction. The junction number is indicated in the picture. The red curve in the inset superimposed to the image is the derivative of the pixel intensity as a function of the vertical position, in this case limited to J_1 and J_2.

absorber layer boundaries were determined as the peak of the spatial derivative of the signal intensity. The layer thickness was then computed as the distance between layer boundary peaks. The thickness values obtained from measurements were averaged over four different regions of one sample to enhance the statistical robustness of the method. The standard deviation for the absorber thickness values ranged between 2 and 6 nm for the junctions J_1 to J_6, and 2–3 nm for the junctions J_7 to J_{10}.

Layer-thickness-optimized design

To establish feasible targets for crystal growers, the total thickness of all absorber layers and the absorber layer thickness of the thickest junction were constrained to below 7 μm and 4 μm, respectively. A two-step procedure was performed by first optimizing layer thicknesses and then determining device performance. First, a layer-thickness optimization was performed using the detailed balance model from Xia and Krich,[26] which includes luminescent coupling but does not include changes in the index of refraction between layers, which can impact luminescent coupling through internal reflections between junctions. Assumptions for the detailed balance model input parameters included an internal radiative efficiency of 0.73 or 0.92 for a τ_{SRH} of 0.11 μs and 3 μs, respectively, no reflection loss, 98% absorption, and 10 W/cm^2 irradiance. We chose the internal radiative efficiency that resulted in a PPC design with the highest drift-diffusion modeled efficiency. These results can be found in Note S3. Then, these optimized absorber thicknesses, calculated from the detailed balance model, were used in our validated drift-diffusion model. For the second step, the antireflection layer thicknesses were optimized and current-voltage properties were simulated with the drift-diffusion model. Note that the efficiencies of the optimized design (τ_{SRH} of 0.11 μs) calculated by our validated drift-diffusion model are up to 8%$_{rel}$ less than the values calculated with the detailed balance model. Unlike our drift-diffusion model, the detailed balance model assumes infinite carrier mobilities and no changes in the index of refraction between layers.

RESOURCE AVAILABILITY

Lead contact

Requests for further information and resources should be directed to and will be fulfilled by the lead contact, Karin Hinzer (khinzer@uottawa.ca).

Material availability

The photonic power converters fabricated in this study are available from the lead contact with a completed materials transfer agreement.

Data and code availability

- All data reported in this paper will be shared by the lead contact upon request.
- All original code for the luminescent coupling model is available at Zenodo: https://doi.org/10.5281/zenodo.15185410. The TCAD Sentaurus project used for simulations within this paper is available at Zenodo: https://doi.org/10.5281/zenodo.15200409.
- Any additional information required to reanalyze the data reported in this paper is available from the lead contact upon request.

ACKNOWLEDGMENTS

We thank Daisy Xia for providing her detailed balance model software. We also thank Simon Fafard and Denis Masson for their advice and loan of a laser. We also thank Erin Tonita for her input on figure aesthetics. Funding was provided by Government of Canada's AI for Design National Research Council Collaborative Science, Technology and Innovation Program under grant INT-014-1, the German Federal Ministry of Education and Research under grant 01DM21006A, the Natural Sciences and Engineering Research Council of Canada (NSERC), the Canadian Foundation for Innovation, and the Government of Ontario.

AUTHOR CONTRIBUTIONS

Conceptualization, G.P.F., D.P.W., M.N.B., C.P., H.H., O.H., D.L., A.W.W., J.J.K., and K.H.; methodology, G.P.F., D.P.W., M.N.B., R.F.H.H., H.H., C.P., D.L., and O.H.; software, G.P.F. and R.F.H.H.; validation, G.P.F., D.P.W., L.-P.S., and C.P.; formal analysis, G.P.F. and C.P.; investigation, G.P.F, D.P.W., M.N.B., C.P., and R.F.H.H.; resources, K.H., D.P., H.H., D.L., and O.H.; data curation, G.P.F., C.P., and R.F.H.H.; writing – original draft, G.P.F; writing – review & editing, G.P.F., D.P.W., M.N.B., C.P., H.H., R.F.H.H., O.H., D.L., Y.G., A.W.W., J.J.K., and K.H.; visualization, G.P.F. and C.P.; supervision, K.H., J.J.K., A.W.W., C.E.V., H.H., O.H., and D.L.; funding acquisition, H.H., K.H., J.J.K., A.W.W., C.E.V., O.H., and D.L.

DECLARATION OF INTERESTS

The authors declare no competing interests.

SUPPLEMENTAL INFORMATION

Supplemental information can be found online at https://doi.org/10.1016/j.xcrp.2025.102610.

Received: September 18, 2024
Revised: March 19, 2025
Accepted: May 2, 2025
Published: May 28, 2025

REFERENCES

1. Matsuura, M. (2021). Recent advancement in power-over-fiber technologies. Photonics *8*, 335.
2. Algora, C., García, I., Delgado, M., Peña, R., Vázquez, C., Hinojosa, M., and Rey-Stolle, I. (2022). Beaming power: Photovoltaic laser power converters for power-by-light. Joule *6*, 340–368.
3. Spillman, W.B., Crowne, D.H., and Woodward, D.W. (1992). Optically powered and interrogated rotary position sensor for aircraft engine control applications. Opt Laser. Eng. *16*, 105–118.
4. Batista De Nazaré, F.V., and Werneck, M.M. (2012). Hybrid optoelectronic sensor for current and temperature monitoring in overhead transmission lines. IEEE Sens. J. *12*, 1193–1194.
5. Worms, K., Klamouris, C., Wegh, F., Meder, L., Volkmer, D., Philipps, S.P., Reichmuth, S.K., Helmers, H., Kunadt, A., Vourvoulakis, J., et al. (2017). Reliable and lightning-safe monitoring of wind turbine rotor blades using optically powered sensors. Wind Energy *20*, 345–360.
6. Goto, K., Nakagawa, T., Nakamura, O., and Kawata, S. (2001). An implantable power supply with an optically rechargeable lithium battery. IEEE Trans. Biomed. Eng. *48*, 830–833.
7. Grandidier, J., Akins, A., Crisp, D., Lee, Y.J., Schwartz, J., Bugga, R., Hall, J.L., Limaye, S., and Brandon, E.J. (2023). Feasibility of power beaming through the Venus atmosphere. Acta Astronaut. *211*, 376–381.
8. Vázquez, C., López-Cardona, J.D., Lallana, P.C., Montero, D.S., Al-Zubaidi, F.M.A., Pérez-Prieto, S., and Garcilópez, I.P. (2019). Multicore fiber scenarios supporting power over fiber in radio over fiber systems. MCF Scenarios Supporting Power Over Fiber in Radio Over Fiber Systems *7*, 158409–158418.
9. Al-Zubaidi, F.M.A., López Cardona, J.D., Sanchez Montero, D., and Vázquez, C. (2021). Optically powered radio-over-fiber systems in support of 5G cellular networks and IoT. J. Lightwave Technol. *39*, 4262–4269.
10. Helmers, H., Armbruster, C., Von Ravenstein, M., Derix, D., and Schöner, C. (2020). 6-W optical power link with integrated optical data Transmission. IEEE Trans. Power Electron. *35*, 7904–7909.
11. Fakidis, J., Helmers, H., and Haas, H. (2020). Simultaneous wireless data and power transfer for a 1-Gb/s GaAs VCSEL and photovoltaic link. IEEE Photonics Technol. Lett. *32*, 1277–1280.
12. Emelyanov, V.M., Pokrovskiy, P.V., Kalyuzhnyy, N.A., Nakhimovich, M.V., and Shvarts, M.Z. (2019). Capacitive characteristics of high-speed photovoltaic converters at combined lighting. Semiconductors *53*, 1959–1963.
13. Fafard, S., and Masson, D.P. (2022). High-efficiency and high-power multijunction InGaAs/InP photovoltaic laser power converters for 1470 nm. Photonics *9*, 438.
14. Fafard, S., and Masson, D.P. (2021). Perspective on photovoltaic optical power converters. J. Appl. Phys. *130*, 160901.
15. Helmers, H., Wagner, L., Garza, C.E., Reichmuth, S.K., Oliva, E., Philipps, S.P., Lackner, D., and Bett, A.W. (2015). Photovoltaic cells with increased voltage output for optical power supply of sensor electronics. In AMA Conferences 2015, Nurnberg, Germany, 2015 (SENSOR), pp. 519–524. https://doi.org/10.5162/SENSOR2015/D1.4.
16. Schubert, J., Oliva, E., Dimroth, F., Guter, W., Loeckenhoff, R., and Bett, A.W. (2009). High-voltage GaAs photovoltaic laser power converters. IEEE Trans. Electron. Dev. *56*, 170–175.
17. Lopez, E., Höhn, O., Schauerte, M., Lackner, D., Schachtner, M., Reichmuth, S.K., and Helmers, H. (2021). Experimental coupling process efficiency and benefits of back surface reflectors in photovoltaic multi-junction photonic power converters. Progress in Photovoltaics. *29*, 461–470.
18. Reichmuth, S.K., Helmers, H., Philipps, S.P., Schachtner, M., Siefer, G., and Bett, A.W. (2017). On the temperature dependence of dual-junction laser power converters. Progress in Photovoltaics. *25*, 67–75.
19. Wandel, E.M. (2006). Attenuation in Silica-Based Optical Fibers (University of Denmark).
20. Crump, P., Erbert, G., Wenzel, H., Frevert, C., Schultz, C.M., Hasler, K.H., Staske, R., Sumpf, B., Maassdorf, A., Bugge, F., et al. (2013). Efficient high-power laser diodes. IEEE J. Sel. Top. Quant. Electron. *19*, 1501211.
21. Vurgaftman, I., Meyer, J.R., and Ram-Mohan, L.R. (2001). Band parameters for III-V compound semiconductors and their alloys. J. Appl. Phys. *89*, 5815–5875.
22. Beattie, M.N., Helmers, H., Forcade, G.P., Valdivia, C.E., Hohn, O., and Hinzer, K. (2023). InP- and GaAs-based photonic power converters under O-band laser illumination: Performance analysis and comparison. IEEE J. Photovoltaics *13*, 113–121.
23. Fafard, S., and Masson, D. (2024). 67.5% Efficient InP-Based Laser Power Converters at 1470 nm at 77 K. Photonics *11*, 130.
24. King, R.R., Bhusari, D., Boca, A., Larrabee, D., Liu, X., Hong, W., Fetzer, C. M., Law, D.C., and Karam, N.H. (2011). Band gap-voltage offset and energy production in next-generation multijunction solar cells. Progress in Photovoltaics. *19*, 797–812.
25. Höhn, O., Walker, A.W., Bett, A.W., and Helmers, H. (2016). Optimal laser wavelength for efficient laser power converter operation over temperature. Appl. Phys. Lett. *108*, 241104.
26. Xia, D., and Krich, J.J. (2020). Efficiency increase in multijunction monochromatic photovoltaic devices due to luminescent coupling. J. Appl. Phys. *128*, 13101.
27. Emelyanov, V.M., Sorokina, S.V., Khvostikov, V.P., and Shvarts, M.Z. (2016). Simulation of the characteristics of InGaAs/InP-based photovoltaic laser-power converters. Semiconductors *50*, 132–137.
28. Friedman, D.J., Geisz, J.F., and Steiner, M.A. (2014). Effect of luminescent coupling on the optimal design of multijunction solar cells. IEEE J. Photovoltaics *4*, 986–990.
29. Steiner, M.A., Geisz, J.F., Moriarty, T.E., France, R.M., McMahon, W.E., Olson, J.M., Kurtz, S.R., and Friedman, D.J. (2013). Measuring IV curves and subcell photocurrents in the presence of luminescent coupling. IEEE J. Photovoltaics *3*, 879–887.
30. Wilkins, M., Valdivia, C.E., Gabr, A.M., Masson, D., Fafard, S., and Hinzer, K. (2015). Luminescent coupling in planar opto-electronic devices. J. Appl. Phys. *118*, 143102.
31. Wilkins, M.M., and Hinzer, K. (2017). Multi-junction solar cells, Chapter 40. Handbook of Optoelectronic Device Modeling and Simulation, *2* (Taylor & Francis).
32. Walker, A.W., Höhn, O., Micha, D.N., Wagner, L., Helmers, H., Bett, A.W., and Dimroth, F. (2015). Impact of photon recycling and luminescence coupling on III–V single and dual junction photovoltaic devices. J. Photon. Energy *5*, 053087.
33. Hui, R., and O'Sullivan, M. (2023). Fiber-Optic Measurement Techniques (Academic Press). https://doi.org/10.1016/B978-0-323-90957-0.00002-3.
34. Forcade, G.P., Beattie, M.N., Valdivia, C.E., Helmers, H., Höhn, O., Wilson, P., St-Arnaud, L.P., Hunter, R., Lackner, D., Krich, J.J., et al. (2023). High-Performance Multi-Junction C-Band Photonic Power Converters: Calibrated Optoelectronic Model for Next Generation Designs. In IEEE 50th Photovoltaic Specialists Conference (PVSC) (IEEE), p. 11. https://doi.org/10.1109/PVSC48320.2023.10359786.
35. Pearce, P. and Liu, V. (2023). S4 - RCWA. GitHub: https://github.com/phoebe-p/S4.
36. Liu, V., and Fan, S. (2012). S4 : A free electromagnetic solver for layered periodic structures. Comput. Phys. Commun. *183*, 2233–2244.
37. Gfroerer, T.H., Cornell, E.A., and Wanlass, M.W. (1998). Efficient directional spontaneous emission from an InGaAs/InP heterostructure with an integral parabolic reflector. J. Appl. Phys. *84*, 5360–5362.
38. Walker, A.W., and Denhoff, M.W. (2017). Heavy and light hole minority carrier transport properties in low-doped n-InGaAs lattice matched to InP. Appl. Phys. Lett. *111*, 162107.
39. Wang, A.-C., Yin, J.-J., Yu, S.-Z., Sun, Y.-R., and Dong, J.-R. (2023). Origins of the short circuit current of a current mismatched multijunction

photovoltaic cell considering subcell reverse breakdown. Opt. Express *31*, 14482–14494.

40. Fafard, S., and Masson, D. (2023). Onset of quantum-confined Stark effects in multijunction photovoltaic laser power converters designed with thin subcells. Photonics *10*, 1243.
41. Geisz, J.F., Friedman, D.J., Steiner, M.A., France, R.M., and Song, T. (2023). Operando temperature measurements of photovoltaic laser power converter devices under continuous high-intensity illumination. IEEE J. Photovoltaics *13*, 808–813.
42. Sotoodeh, M., Khalid, A.H., and Rezazadeh, A.A. (2000). Empirical low-field mobility model for III-V compounds applicable in device simulation codes. J. Appl. Phys. *87*, 2890–2900.
43. Lumb, M.P., Yakes, M.K., and González, M. (2013). Optical properties of Si-doped and Be-doped InAlAs lattice-matched to InP grown by molecular beam epitaxy. J. Appl. Phys. *114*, 103504.
44. Bardyszewski, W., and Yevick, D. (1985). Compositional dependence of the Auger coefficient for InGaAsP lattice matched to InP. J. Appl. Phys. *58*, 2713–2723.
45. Schygulla, P., Fuß-Kailuweit, P., Höhn, O., and Dimroth, F. (2020). Determination of the complex refractive index of compound semiconductor alloys for optical device modelling. J. Phys. D Appl. Phys. *53*, 495104.
46. Helmers, H., Karcher, C., and Bett, A.W. (2013). Bandgap determination based on electrical quantum efficiency. Appl. Phys. Lett. *103*, 32108.
47. McIntosh, K.R. (2001). Lumps, Humps and Bumps : Three Detrimental Effects in the Current-Voltage Curve of Silicon Solar Cells (University of New South Wales). https://doi.org/10.26190/UNSWORKS/4284.
48. Ahrenkiel, R.K., Keyes, B.M., and Dunlavy, D.J. (1991). Intensity-dependent minority-carrier lifetime in III-V semiconductors due to saturation of recombination centers. J. Appl. Phys. *70*, 225–231.
49. Walker, A.W., Heckelmann, S., Karcher, C., Höhn, O., Went, C., Niemeyer, M., Bett, A.W., and Lackner, D. (2016). Nonradiative lifetime extraction using power-dependent relative photoluminescence of III-V semiconductor double-heterostructures. J. Appl. Phys. *119*, 155702.
50. Melati, D., Grinberg, Y., Kamandar Dezfouli, M., Janz, S., Cheben, P., Schmid, J.H., Sánchez-Postigo, A., and Xu, D.X. (2019). Mapping the global design space of nanophotonic components using machine learning pattern recognition. Nat. Commun. *10*, 4775.
51. Saive, R., Borsuk, A.M., Emmer, H.S., Bukowsky, C.R., Lloyd, J.V., Yalamanchili, S., and Atwater, H.A. (2016). Effectively Transparent Front Contacts for Optoelectronic Devices. Adv. Opt. Mater. *4*, 1470–1474.
52. Nouri, N., Valdivia, C.E., Beattie, M.N., Krich, J.J., and Hinzer, K. (2022). Light management in ultra-thin photonic power converters for 1310 nm laser illumination. Opt. Express *30*, 23417–23427.
53. Helmers, H., Lopez, E., Höhn, O., Lackner, D., Schön, J., Schauerte, M., Schachtner, M., Dimroth, F., and Bett, A.W. (2021). 68.9% Efficient GaAs-based photonic power conversion enabled by photon recycling and optical resonance. Physica Rapid Research Ltrs. *15*, 2100113.
54. Horowitz, K. A. W., Remo, T., Smith, B. & Ptak, A. A Techno-Economic Analysis and Cost Reduction Roadmap for III-V Solar Cells. https://www.nrel.gov/docs/fy19osti/72103.pdf. (2018).
55. Schygulla, P., Klitzke, M., Höhn, O., Predan, F., Lackner, D., Schön, J., Tibbits, T., Helmers, H., and Dimroth, F. (2022). Increasing transferability between design and epitaxial growth of multi-junction solar cells. In 17th International Conference on Concentrator Photovoltaic Systems, pp. 020009. https://doi.org/10.1063/5.0099724.
56. Oliva, E., Dimroth, F., and Bett, A.W. (2008). GaAs converters for high power densities of laser illumination. Progress in Photovoltaics. *16*, 289–295.
57. Beattie, M. (2021). Semiconductor Materials and Devices for High Efficiency Broadband and Monochromatic Photovoltaic Energy Conversion (University of Ottawa). https://doi.org/10.20381/ruor-26695.
58. Soresi, S., Hamon, G., Larrue, A., Alvarez, J., Pires, M.P., and Decobert, J. (2018). InP:S/AlInAs:C tunnel junction grown by MOVPE for photovoltaic applications. Phys. Status Solidi *215*, 1700427.
59. Adachi, S. (1989). Optical dispersion relations for GaP, GaAs, GaSb, InP, InAs, InSb, AlxGa1−xAs, and In1−xGaxAsyP1−y. J. Appl. Phys. *66*, 6030–6040.
60. Dinges, H.W., Burkhard, H., Lösch, R., Nickel, H., and Schlapp, W. (1992). Refractive indices of InAlAs and InGaAs/InP from 250 to 1900 nm determined by spectroscopic ellipsometry. Appl. Surf. Sci. *54*, 477–481.
61. Herzinger, C.M., Snyder, P.G., Johs, B., and Woollam, J.A. (1995). InP optical constants between 0.75 and 5.0 eV determined by variable-angle spectroscopic ellipsometry. J. Appl. Phys. *77*, 1715–1724.
62. Anderson, W.W. (1980). Absorption constant of Pb1-xSnxTe and Hg1-xCdxTe alloys. Infrared Phys. *20*, 363–372.
63. Hahn, D., Jaschinski, O., Wehmann, H.-H., Schlachetzki, A., and Von Ortenberg, M. (1995). Electron-concentration dependence of absorption and refraction in n-In0.53Ga0.47As near the band-edge. J. Electron. Mater. *24*, 1357–1361.
64. Gozu, S., Mozume, T., and Ishikawa, H. (2008). Refractive index of Si-doped-InGaAs. J. Appl. Phys. *104*, 073507.
65. Amiotti, M., and Landgren, G. (1993). Ellipsometric determination of thickness and refractive index at 1.3, 1.55, and 1.7 μm for In(1−x)GaxAsyP(1−y) films on InP. J. Appl. Phys. *73*, 2965–2971.
66. Muñoz, M.M., Holden, T.M., and Pollak, F.H. (2002). Optical constants of InGaAs/InP: Experiment and modeling. J. Appl. Phys. *92*, 5878.
67. Humphreys, D.A. (1985). Measurement of absorption coefficients of Ga0.47In0.53As over the wavelength range 1.0-1.7 um. Electron. Lett. *21*, 1187–1189.
68. Zielinski, E., Schweizer, H., Streubel, K., Eisele, H., and Weimann, G. (1986). Excitonic transitions and exciton damping processes in InGaAs/InP. J. Appl. Phys. *59*, 2196–2204.
69. Bacher, F.R., Blakemore, J.S., Ebner, J.T., and Arthur, J.R. (1988). Optical-absorption coefficient of In1-xGaxAs/InP. Phys. Rev. B *37*, 2551–2557.
70. Aspnes, D.E., and Studna, A.A. (1983). Dielectric functions and optical parameters of Si, Ge, GaP, GaAs, GaSb, InP, InAs, and InSb from 1.5 to 6.0 eV. Phys. Rev. B *27*, 985–1009.
71. Seifert, S., and Runge, P. (2016). Revised refractive index and absorption of InGaAsP lattice-matched to InP in transparent and absorption IR-region. Opt. Mater. Express *6*, 251691.
72. Wang, A.C., Sun, Y.R., Yu, S.Z., Yin, J.J., Zhang, W., Wang, J.s., Fu, Q.X., and Dong, J.R. (2021). A method to analyze current mismatch in a multi-junction laser power converter based on I-V measurements. Appl. Phys. Lett. *118*, 233902.
73. Schauerte, M., Höhn, O., and Helmers, H. (2022). Subcell spectral response determination for multi-junction photonic power converters based on negative bias I-V measurements. In 4th Optical Wireless and Fiber Power Transmission Conference.

Cell Reports Physical Science, Volume *6*

Supplemental information

Multi-junction laser power converters exceeding 50% efficiency in the short wavelength infrared

Gavin P. Forcade, D. Paige Wilson, Meghan N. Beattie, Carmine Pellegrino, Henning Helmers, Robert F.H. Hunter, Oliver HÖhn, David Lackner, Louis-Philippe St-Arnaud, Thomas N.D. Tibbits, Daniel Poitras, Christopher E. Valdivia, Yuri Grinberg, Alexandre W. Walker, Jacob J. Krich, and Karin Hinzer

Note S1. Single-junction measurements and model validation

We fabricated three single-junction photovoltaic isotypes with varying $In_{0.53}Ga_{0.47}As$ absorber layer thicknesses lattice-matched to InP at Fraunhofer Institute for Solar Energy Systems. We use a four-wire configuration to measure the current density–voltage (*J-V*) characteristics of each photovoltaic device in the dark and under 1.52 µm laser illumination, sweeping the voltage in both directions and taking the average, with results shown in Figure S1A. Of all the three samples, we measure hysteresis only on the 180 nm thick absorber device. We measure each device's reflectivity and external quantum efficiency (*EQE*) using an Oriel IQE200, with results shown in Figure S1B and S1C. We select the devices with the lowest dark current at -0.02 V from each sample and use them to calibrate our drift-diffusion model.

We apply the same model for the single-junction devices as for the ten-junction devices. However, for the single-junction devices, we also include trap-assisted and band-to-band tunneling to better fit the dark *J-V* curves in reverse bias.[1]

To validate and acquire parameters for our model, we calculate the root-mean-square-relative difference between measured and simulated results for both the dark *J-V* and spectral reflectivity. We use Python's SciPy SLSQP optimizer to minimize the sum of those two root-mean-square values with the fits shown in Figure S1A and S1B. We vary layer thicknesses, absorber layer SRH lifetime, absorber layer Huang-Rhys factor for the trap-assisted tunneling, series resistance, and the peak position and standard deviation of the Gaussian p-doping profile. In addition, we include an EQE and reflectivity multiplicity factor to account for shading from the gridlines. The optimizer reached layer thicknesses within 10% of the targeted growth values. The SRH recombination lifetime was fit to 3 ± 2 µs, which aligns with the measured values of 1.7-2.6 µs from references.[2,3] The Huang-Rhys factor of 8 ± 3 is comparable to a previously published value of 6.8.[1] A 0.01 Ω resistor in series with the device was used for the fits, bending the dark *J-V* at the highest forward bias voltages. The fitted EQE and reflectivity multiplicity factor is 0.97±0.01.

Our model describes the single-junction devices well, as seen in Figure S1A and S1B, which compares simulated fits to measurements for three samples with different absorber thicknesses; other samples show similar results. At far reverse bias, band-to-band tunneling dominates and is adjusted in the model by the doping profile. The tunneling is also affected by the absorber thickness. At small reverse and forward biases, trap-assisted tunneling and/or SRH

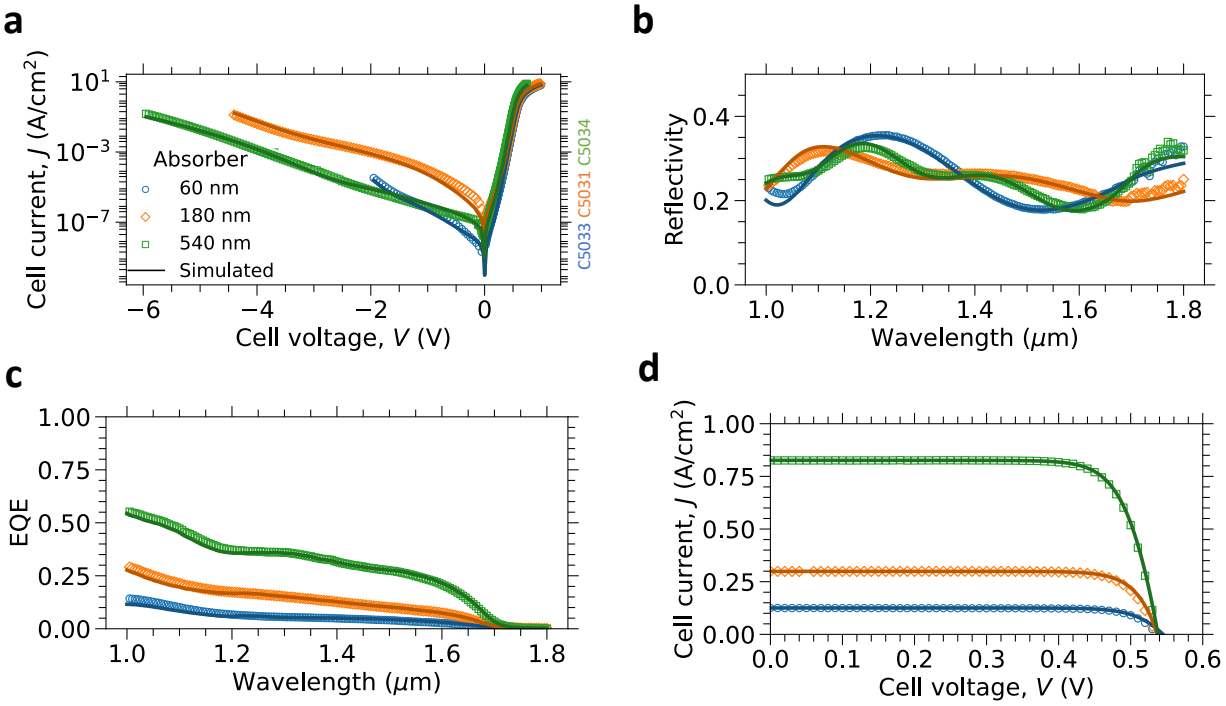

Figure S1. Single-junction photonic power converter isotypes characterized.
Measured (empty markers) and simulated (lines) **a** dark *J-V*, **b** reflectivity, **c** external quantum efficiency, and **d** light *J-V* curves. Simulated optoelectronic model curves are fit to our measured data. The legend provides the device's absorber layer thickness. The light *J-V* curves are measured under 2.66 W/cm² incident 1.52 µm laser powers.

generation prevails, tuned by the SRH lifetime and the Huang-Rhys factor. The 180 nm device exhibited a significant trap-assisted tunneling current in reverse bias, evident from the few orders of magnitude larger current at around -2 V. We attribute the small discrepancy near 0 V for the 180 nm device in Figure 1A to hysteresis effects, which could arise from traps around the perimeter of the device. At large forward bias, radiative recombination dominates, highlighting the quality of the epi-growth. Finally, series resistance throttles current above 0.5 A/cm^2. The FSF and absorber layer thicknesses dominate the reflectivity curve fitting shown in Figure S1B. We attribute the discrepancy for wavelengths larger than 1.7 µm to measurement noise due to the lower sensitivity of the Ge detector in our instrument.

We further validate our model by comparing simulated to measured *EQE* and light *J-V* in Fig. S1C and S1D. The root-mean-square difference between measured and simulated EQE is within 1%, which supports our method of extracting the extinction coefficient for InGaAs (see "Methods" in the main article). For the light *J-V* properties, we match the short-circuit current density to the measured value by varying the input power. The resulting simulated input powers are within 4% of the measured values.

Note S2. No luminescence coupling during reverse bias measurement

Luminescent coupling can increase the current of current-limiting junctions in multi-junction devices. We check for luminescent coupling during our reverse bias method of extracting absorber layer thicknesses as the method relies on a deliberately produced current mismatch between the junctions to create steps in reverse bias. Extracting layer thicknesses from those steps requires assuming they are the photogenerated currents of junctions without luminescent coupling contribution. We can employ the fact that luminescent coupling should increase with input power to assess its presence.[4] We demonstrate the absence of luminescent coupling by measuring the I-V curve in reverse bias for several 1.31 µm laser illumination powers (equal to and larger than our reverse-bias-method power of 1.7 mW). We then calculate the spectral response (junction short-circuit current divided by input power) of each junction, assuming the current at the plateaus is the short-circuit current of the junctions, with the results shown in Figure S2. As the spectral responses of all the junctions are flat within our measurement uncertainty, we conclude that luminescent coupling is insignificant for these measurements.

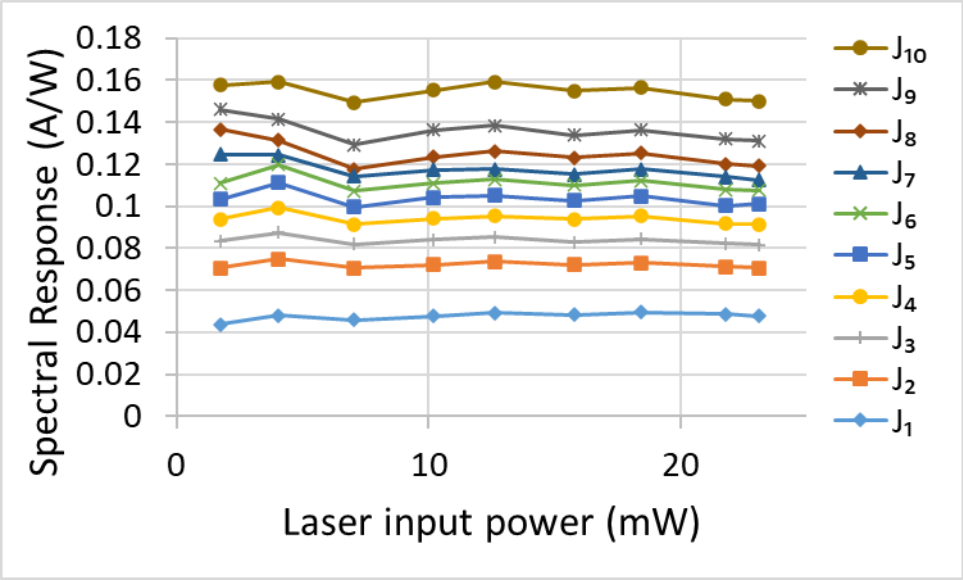

Figure S2. Luminescent coupling investigation.
Spectral response of each junction in the ten-junction InGaAs photonic power converter as a function of 1.31 µm laser input power. J_{10} is the top junction.

Note S3. Detailed balance model: choosing the internal radiative efficiency

To predict luminescent-coupling-optimized layer thicknesses, we employ the detailed balance model from Xia and Krich.[5] We assume an irradiance of 10 W/cm^2, an absorption of 98%, and InGaAs's complex refractive index and

bandgap with the same values that we use in our drift-diffusion model. We also implement the absorber thickness constraints: the total thickness of all absorber layers below 7 µm and the absorber layer thickness of the thickest junction below 4 µm. The detailed balance model runs quickly, permitting optimization for layer thicknesses. We then implement those thicknesses into our calibrated drift-diffusion model, which includes finite carrier mobilities and varying refractive indexes between materials, to assess the PPC's performance.

The detailed balance model requires an internal radiative efficiency (IRE) value. The detailed balance model contains the physics of luminescent coupling but does not have the correct physics for transport and optical propagation. We, therefore, use it to create a one-parameter family of device thicknesses, all of which take advantage of luminescent coupling. We artificially vary the IRE of the absorber material in the detailed balance model and find the optimized layer thicknesses for each IRE. While the detailed balance efficiency increases monotonically with IRE, we use these optimized thicknesses in the drift-diffusion model to calculate the efficiency of the PPC device; the results are provided in Figure S3. The black symbols indicate internal radiative efficiency values of 0.73 and 0.91 and produce layer thicknesses that maximize drift-diffusion efficiencies for τ_{SRH} values of 0.11 µs and 3 µs, respectively.

Note that the IRE can also be calculated at the maximum power point from the drift-diffusion model by considering the fraction of radiative losses; that calculation gives 0.5 and 0.92 for the two structures. For τ_{SRH} of 3 µs, the IRE from the drift-diffusion model is within 1% of the IRE in the detailed balance calculations that produce layer thicknesses with maximum drift-diffusion efficiency. This agreement makes sense and is what we expect if the key physics of the two models agree. However, when τ_{SRH} is 0.11 µs, the drift-diffusion IRE at maximum power is 0.5, while the detailed balance IRE of 0.73 produces layer thicknesses with the highest power. Neither of these IRE's is strongly radiative, and Figure S3 shows that the change of efficiency with the detailed balance IRE is quite small. Since the device does not have strong luminescent coupling, we cannot expect perfect agreement in the IREs from these methods.

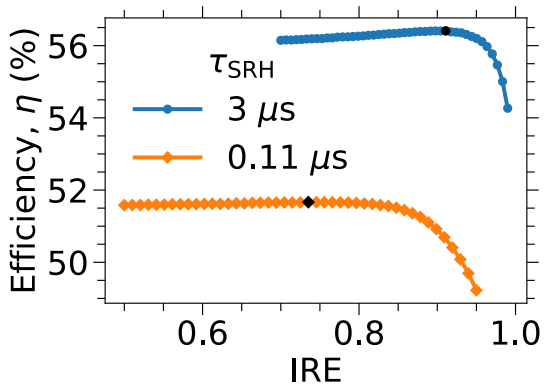

Figure S3. Impact of internal radiative efficiency on design performance.
The efficiency of luminescent coupling-optimized devices calculated by the drift-diffusion model with absorber layer thicknesses provided by the detailed balance model as a function of the input internal radiative efficiency (IRE) values. The black symbols indicate the maximum value.

Note S4. Layer-thickness-optimized designs outperform absorption-matched designs

We simulate the optoelectronic performance of the layer-thickness-optimized design and compare it to an identical InGaAs ten-junction design with absorption-matched layer thicknesses calculated using rigorous coupled wave analysis. The efficiency and maximum power point voltage gains achieved by the layer-thickness-optimized design as a function of irradiance are shown in Figure S4 (dashed curve) for a 1.52 µm laser wavelength. Compared to the absorption-matched design, the layer-thickness-optimized design gains up to 0.25%$_{rel}$ in efficiency and up to 0.2% in the maximum power point voltage assuming a τ_{SRH} of 0.11 µs.

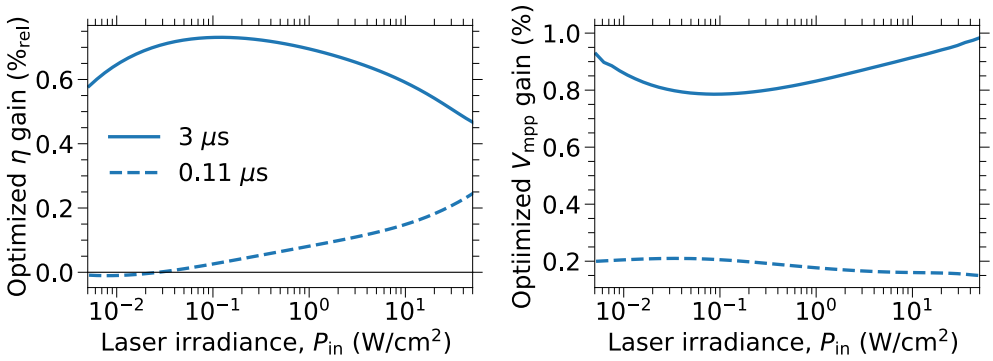

Figure S4. Layer-thickness-optimized designs outperform absorption-matched designs
Efficiency (left) and voltage (right) at maximum power point of ten-junction InGaAs PPCs with layer-thickness-optimized designs relative to absorption-matched designs as a function of 1.52 μm laser irradiance. We explore two material qualities, τ_{SRH} of 0.11 μs and 3 μs.

For luminescent coupling to significantly enhance performance, we require a much longer τ_{SRH} than the radiative lifetime.[5] We calculated a radiative lifetime within the absorber layer of 0.8 μs using the model presented in Roosbroeck and Shockley with our measured absorption coefficients and absorber doping concentration.[6] Therefore, we also investigate the performance gains from a new layer-thickness-optimized design using a τ_{SRH} of 3 μs, representing our average material quality for single-junction isotype cells. This PPC shows greater performance gains than the PPC designed for lower-quality material, as was suggested in Ref.[7]. Also, the layer-thickness-optimized design outperforms the absorption-matched design across the entire range of irradiance we explore (solid curve in Figure S4). Efficiency gains can reach up to 0.75%$_{rel}$, while output voltage gains can be up to 1%.

Note S5. Number of junctions versus bandgap

For a single-junction device, the open-circuit voltage (V_{oc}) can be related to its absorber material's bandgap (E_g) by:[8,9]

$$V_{oc,1} = \frac{E_g}{q} - W_{oc,1} \qquad (S1)$$

where $W_{oc,1}$ is the bandgap-voltage offset at open-circuit voltage and is a parameter indicating the quality of the material. However, to maximize PPC efficiency, the devices must operate at the maximum power point with a voltage $V_{mpp,1}=aV_{oc,1}$. Assuming a similar relation as Eq. S1 for $V_{mpp,1}$, we can rearrange to relate the bandgap-voltage offset at maximum power point ($W_{mpp,1}$) to E_g, a, and $W_{oc,1}$ as follows:

$$W_{mpp,1} = \frac{E_g}{q}(1-a) + aW_{oc,1} \qquad (S2)$$

For a multi-junction device with N similar subcells, we can sum up the contributions from each subcell to get the total device output voltage at open-circuit:

$$V_{oc,N} = \sum_i^N V_{oc,i} = \left(\frac{E_g}{q} - W_{oc,1}\right) N \qquad (S3)$$

For dissimilar junctions, which is generally the case, Eq. S3 averages the open-circuit voltage and then multiplies that voltage by the number of junctions. Combining Eq. S3 (but with "mpp" instead of "oc") with Eq. S2, we get:

$$V_{mpp,N} = \left(\frac{E_g}{q} - \left(\frac{E_g}{q}(1-a) + aW_{oc,1}\right)\right) N = \left(\frac{E_g}{q} - W_{oc,1}\right) aN \qquad (S4)$$

To extract a and $W_{oc,1}$, we iterate a two-step fitting procedure targeting $V_{mpp,N}$ = 5 V and fitting to simulation results from our drift-diffusion model, assuming a Shockley-Read-Hall lifetime of 0.11 μs, a 10 W/cm^2 irradiance from a laser with photon energy 30 meV larger than the absorber bandgap. First, we fit Eq. S3 to our calculated drift-diffusion

model data assuming an initial value of a = 0.9 ($V_{oc,N}$ = 5.6 V) and extract a value for $W_{oc,1}$. Second, we fit Eq. S4 to drift-diffusion data for $V_{mpp,N}$ = 5 V using the fitted value of $W_{oc,1}$ and the initial value of a. We iterated over these two steps to minimize the root-mean-square difference between the drift-diffusion data assuming $V_{mpp,N}$ = 5 V and Eq. S4 data. The fitting results for the V_{oc} and V_{mpp} data are shown in Figure S5A and S5B, respectively. The final fitted values are a = 0.88 and $W_{oc,1}$ = 0.185 V. The slight offset at high absorber bandgaps in Figure S5A could come from a $W_{oc,1}$ with bandgap dependence. The bandgap dependence could arise from differences in current production (since we assumed a constant irradiance but photon energy that is 30 meV larger than the bandgap), non-radiative recombination, and/or absorber layer thicknesses.

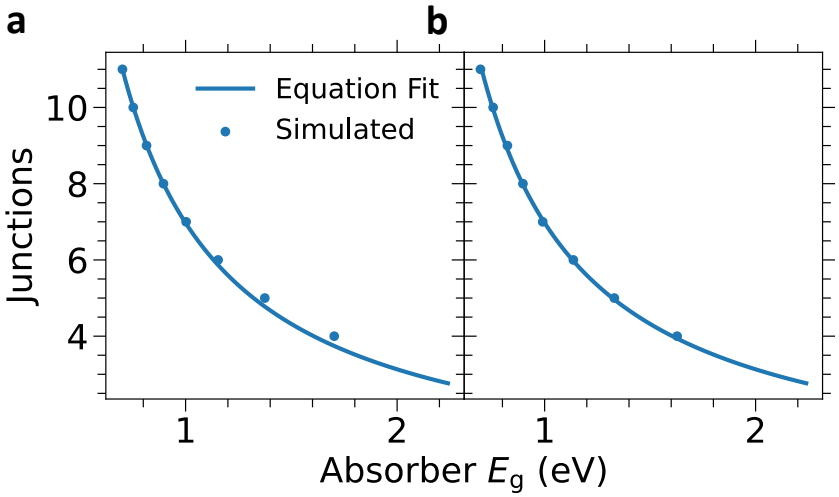

Figure S5. Number of junctions required to reach 5 V at maximum power for a given absorber bandgap.
We compare the fitted Eq. S3 (**a**) and Eq. S4 (**b**) to the values calculated from drift-diffusion simulation results.

Note S6. Additional Four-Junction InGaAsP PPC characteristics

The four-junction InGaAsP photonic power converters exhibit excellent stability. We measured the current at a voltage of 2.176 V for approximately 120 seconds under illumination from a 1.446 µm laser with an input power of 15.1 W/cm^2, as shown in Figure S6A. These voltage and irradiance values correspond to the maximum efficiency values of the best device. To achieve faster temporal resolution, the number of power line cycles (NPLC) of the Keithley instrument was reduced to 0.01 for this measurement. After about one second, the beam blocker was removed, resulting in an initial current of approximately 3.75 A/cm^2, which decreased to 3.73 A/cm^2 after around 0.4 seconds due to device heating. This initial current boost should not affect our measured efficiency values, as the current-voltage measurements take at least 2 seconds and start at 0 V (with the maximum power point close to open-circuit voltage). We also measured spectral reflectivity, with results shown in Figure S6B.

The four-junction InGaAsP photonic power converters demonstrate excellent performance across multiple devices. We measured the current-voltage characteristics of 10 devices randomly selected across a quartile of single substrate (including a device ¼" from the 4" wafer's edge) at an input power of 15.1 W/cm^2 using the 1.446 µm laser, with results shown in Figure S6C. The essential parameters from the current-voltage curves are presented in Figure S6D as box and whisker plots, including efficiency, short-circuit current density, open-circuit voltage, and fill factor. Note that the irradiance for measurements shown in Figure S6 was 0.1 W/cm^2 less than the highest efficiency irradiance in Figure 6 of the main manuscript as the system was realigned for Figure S6 results.

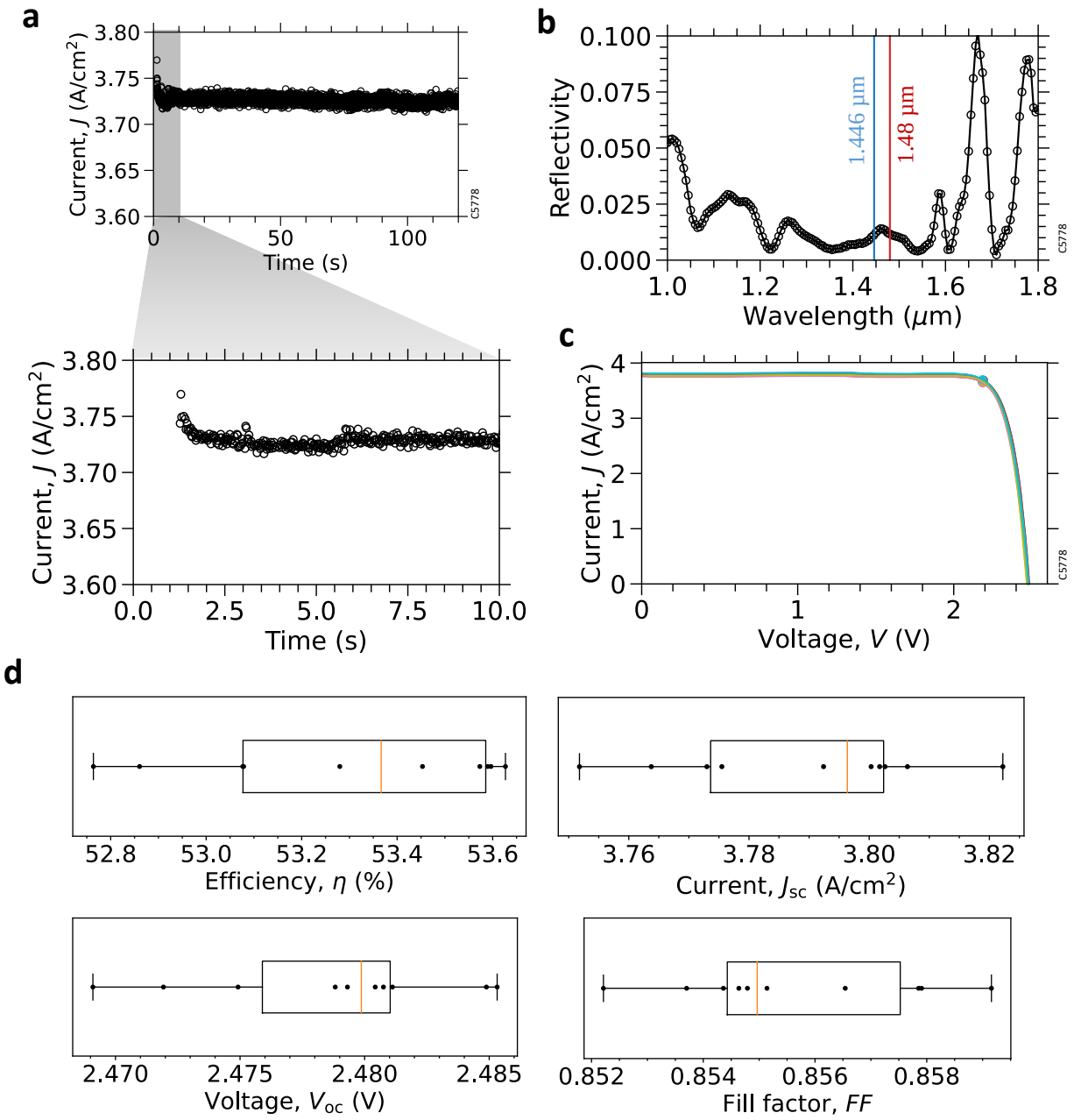

Figure S6. Four-junction InGaAsP device characterization.
(a) Measured current at an applied forward bias voltage of 2.176 V as a function of time illuminated at 15.1 W/cm^2 with the 1.446 µm laser. The plot below zooms in on the time axis to show the initial current boost. The beam blocker for this measurement was taken out at about 1 s. (b) Measured spectral reflectivity. (c) Current-voltage curves of 10 devices, from a single substrate, when illuminated at an input power of 15.1 W/cm^2 with the 1.446 µm laser. The circle symbols mark the maximum power points. (d) Box and whisker plots of the efficiency, short-circuit current density, open-circuit voltage, and fill factor extracted from the curves in (c). The box represents the 25th and 75th percentiles, and the whiskers are the minimum and maximum values. The black points are the data points from the 10 devices.

References

1. Aspnes, D. E. & Studna, A. A. Dielectric functions and optical parameters of Si, Ge, GaP, GaAs, GaSb, InP, InAs, and InSb from 1.5 to 6.0 eV. *Phys Rev B* **27**, (1983).
2. Adachi, S. Optical dispersion relations for GaP, GaAs, GaSb, InP, InAs, InSb, AlxGa1−xAs, and In1−xGaxAsyP1−y. *J Appl Phys* **66**, 6030–6040 (1989).
3. Seifert, S. & Runge, P. Revised refractive index and absorption of InGaAsP lattice-matched to InP in transparent and absorption IR-region. *Opt Mater Express* **6**, 251691 (2016).
4. Dinges, H. W., Burkhard, H., Losch, R., Nickel, H. & Schlapp, W. Refractive indices of InAlAs and InGaAs/InP from 250 to 1900 nm determined by spectroscopic ellipsometry. *Appl Surf Sci* **54**, 477–481 (1992).
5. Gozu, S., Mozume, T. & Ishikawa, H. Refractive index of Si-doped-InGaAs. *J Appl Phys* **104**, (2008).
6. Amiotti, M. & Landgren, G. Ellipsometric determination of thickness and refractive index at 1.3, 1.55, and 1.7 μm for In(1−x)GaxAsyP(1−y) films on InP. *J Appl Phys* **73**, 2965 (1992).
7. Muñoz, M. M., Holden, T. M. & Pollak, F. H. Optical constants of Experiment and modeling ARTICLES YOU MAY BE INTERESTED IN. *J Appl Phys* **92**, 5878 (2002).
8. Hahn, D., Jaschinski, O., Wehmann, H.-H., Schlachetzki, A. & Von Ortenberg, M. Electron-Concentration Dependence of Absorption and Refraction in n-lno.53Gao.47As Near the Band-Edge. *J Electron Mater* **24**, (1995).
9. Humphreys, D. A. Measurement of absorption coefficients of Ga0.47In0.53As over the wavelength range 1.0-1.7 um. *Electron Lett* **21**, (1985).
10. Zielinski, E., Schweizer, H., Streubel, K., Eisele, H. & Weimann, G. Excitonic transitions and exciton damping processes in InGaAs/InP. *J Appl Phys* **59**, 2196 (1998).
11. Bacher, F. R., Blakemore, J. S., Ebner, J. T. & Arthur, J. R. Optical-absorption coefficient of In1-xGaxAs/InP. *Phys Rev B* **37**, 2551–2557 (1988).
12. Schygulla, P., Fuß-Kailuweit, P., Höhn, O. & Dimroth, F. Determination of the complex refractive index of compound semiconductor alloys for optical device modelling. *J Phys D Appl Phys* **53**, 8 (2020).
13. Anderson, W. W. Absorption constant of Pb1-xSnxTe and Hg1-xCdxTe alloys. *Infrared Phys* **20**, 363–372 (1980).
14. Schenk, A. & Sant, S. Tunneling between density-of-state tails: Theory and effect on Esaki diodes. *J Appl Phys* **128**, (2020).
15. Gfroerer, T. H., Cornell, E. A. & Wanlass, M. W. Efficient directional spontaneous emission from an InGaAs/InP heterostructure with an integral parabolic reflector. *J Appl Phys* **84**, 5360–5362 (1998).
16. Walker, A. W. & Denhoff, M. W. Heavy and light hole minority carrier transport properties in low-doped n-InGaAs lattice matched to InP. *Appl. Phys. Lett* **111**, 162107 (2017).
17. Wang, A. C. *et al.* A method to analyze current mismatch in a multijunction laser power converter based on I-V measurements. *Appl Phys Lett* **118**, 233902 (2021).
18. Xia, D. & Krich, J. J. Efficiency increase in multijunction monochromatic photovoltaic devices due to luminescent coupling. *J Appl Phys* **128**, 13101 (2020).
19. King, R. R. *et al.* Band gap-voltage offset and energy production in next-generation multijunction solar cells. *Progress in Photovoltaics: Research and applications* **19**, 797–812 (2011).
20. Beattie, M. N. *et al.* InP- and GaAs-based photonic power converters under O-band laser illumination: Performance analysis and comparison. *IEEE J Photovolt* **13**, 113–121 (2023).